Journal of Geophysical Research: Space Physics

RESEARCH ARTICLE
10.1029/2017JA025038

Key Points:
- Linear regression can account for the background variability and Energetic Particle Precipitation (EPP) impact on mesospheric hydroxyl (OH)
- The OH variability is mainly driven by changes in temperature and H_2O above 70-km altitude and by EPP below 70-km altitude
- Protons dominate over electrons below 70-km altitude, but the electron impact is comparable to that of protons above 70-km altitude

Correspondence to:
A. E. Zawedde,
Annet.E.Zawedde@uib.no

Citation:
Zawedde, A. E., Nesse Tyssøy, H., Stadsnes, J., & Sandanger, M. I. (2018). The impact of energetic particle precipitation on mesospheric OH – Variability of the sources and the background atmosphere. *Journal of Geophysical Research: Space Physics*, *123*. https://doi.org/10.1029/2017JA025038

Received 22 NOV 2017
Accepted 4 JUN 2018
Accepted article online 12 JUN 2018

The Impact of Energetic Particle Precipitation on Mesospheric OH – Variability of the Sources and the Background Atmosphere

Annet Eva Zawedde[1], Hilde Nesse Tyssøy[1], Johan Stadsnes[1], and Marit Irene Sandanger[1]

[1] Birkeland Centre for Space Science, Department of Physics and Technology, University of Bergen, Bergen, Norway

Abstract Using a new analysis technique, we estimate the precipitating particle fluxes measured by the Medium Energy Proton and Electron Detector on the National Oceanic and Atmospheric Administration Polar Orbiting Environmental Satellites. These fluxes are used to quantify the direct impact of energetic particle precipitation (EPP) on mesospheric hydroxyl (OH) measured from the Aura satellite during 2005–2009 in the Northern Hemisphere, covering the declining and minimum phase of solar cycle 23. Using multiple linear regression of nighttime OH volume mixing ratio with temperature, geopotential height, water vapor (H_2O) volume mixing ratio, Lyman-alpha (Ly-α) radiation, and particle energy deposition, we account for the background variability and hence the EPP impact independent of season and other short-term variability. We investigate the relative importance of solar proton events, energetic electron precipitation and the background to OH variability. The background dominates over EPP above 70-km altitude. Below 70 km, EPP dominates. The maximum EPP contribution is 44% and 34% in the geographic and corrected geomagnetic (CGM) settings respectively at 67 km. Protons dominate over electrons at mesospheric altitudes with maximum contributions of 43% and 32% at 67 km in the geographic and CGM settings, respectively. In a CGM setting, the electrons contribution is comparable to that of protons above 70 km, with a maximum contribution of 11% at 75 km. Since the period investigated is during relatively low solar activity, these results represent a lower estimate of the general EPP contribution to OH variability.

1. Introduction

In the mesosphere, background odd hydrogen (HO_X: H, OH, HO_2) is produced by photodissociation of water vapor (H_2O) by the reaction (Brasseur & Solomon, 2005; Solomon et al., 1981; Swider & Keneshea, 1973):

$$H_2O + h\nu \rightarrow H + OH \quad (1)$$

The photolysis of H_2O is facilitated by the Lyman-alpha (Ly-α) line (121.568 nm) for altitudes above 68 km and by Schumann-Runge band wavelengths (175–200 nm) at altitudes 60–68 km (Frederick & Hudson, 1980). The background OH production is also modified by the seasonal pole to pole circulation pattern as it affects both H_2O and temperature. Hence, the OH seasonal variability can be largely understood by considering the variations in H_2O and solar intensity (see, e.g., Canty & Minschwaner, 2002; Shapiro et al., 2012). The amount of solar radiation at a specific altitude and latitude varies with the solar zenith angle (SZA). As such the diurnal variations in OH can be described by an exponential function of the secant of the SZA (Minschwaner et al., 2011).

The wintertime OH background production is also affected by processes involving planetary wave activity, like sudden stratospheric warmings (SSWs) through an associated descent of the OH layer (see, e.g., Damiani et al., 2010; Winick et al., 2009; Zawedde et al., 2016). For example, normally OH would have a positive correlation with H_2O, and a corresponding negative correlation with temperature. However, during SSWs OH seems to have a negative correlation with H_2O and a positive correlation with temperature as elevated temperature is associated with adiabatic heating due to downwelling bringing dry air downward (see, e.g., Damiani et al., 2010). Therefore, simple correlation alone is not enough to ascertain the relation between OH and the related atmospheric constituents.

Energetic particle precipitation (EPP) is known to produce HO_X during solar proton events (SPEs) and energetic electron precipitation (EEP). SPEs are associated with strong geomagnetic activity driven by coronal mass ejections (CMEs) which predominantly occur during solar maximum (see, e.g., Webb, 1995). CMEs propel fast shock waves ahead of them which accelerate solar protons directly from the solar wind to very high energies capable of precipitating into the atmosphere to ~40-km altitude over the polar cap on open field lines. Depending on the particle energy, the solar protons can also penetrate closed field lines and impact the atmosphere at latitudes normally shielded from the direct solar wind impact. Monoenergetic beams of protons of energy 10-20 MeV will deposit most of their energy within the mesosphere (60-80 km) (Turunen et al., 2009). On the other hand, energetic electrons are first stored and accelerated in the Earth's radiation belts. During geomagnetic storms, electrons are accelerated to high and possibly relativistic energies before precipitating into the atmosphere (see, e.g., Li & Temerin, 2001; Reeves et al., 2013; Turner et al., 2012). Clear effects of electron precipitation on OH are seen within the latitude range of the Earth's radiation belts at magnetic latitudes 55–72° (see, e.g., Andersson, Verronen, Rodger, Clilverd, & Wang 2014). This is a small band within the atmosphere as compared to the polar cap where the protons deposit their energy. Medium energy and relativistic electrons (>100 keV) precipitate below 80 km (Turunen et al., 2009).

On interpreting the results from Weeks et al. (1972), Swider and Keneshea (1973) state that during ionization events, for every O_2^+ ion converted into an oxonium (water cluster) ion, one OH molecule is generated. An additional contribution will arise from dissociative recombination of the water cluster ions with electrons, yielding either H or OH as one of the reaction products. Therefore, the total OH + H formation rate resulting from the water cluster ion formation can be seen as $2HO_X$ (Solomon et al., 1981). Also, the behavior of the perhydroxyl radical (HO_2) is generally similar to OH (see Crutzen & Solomon, 1980). This implies that we can focus on one of the constituents in the HO_X family (i.e., OH) to study the effects of EPP on the atmospheric system.

The Aura Microwave Limb Sounder (MLS) database provides observations of both OH and HO_2, although the MLS HO_2 data are not recommended for scientific use for altitudes above 0.046 hPa (~70 km) (Livesey et al., 2015. The availability of Aura MLS OH observations sparked the genesis of several correlation studies between OH and particle fluxes. These studies have attempted to estimate how much of the mesospheric OH variability can be attributed to both SPEs and EEP. Since SPEs are strong, their effects on the atmospheric constituents are easily detected and have been extensively studied (Crutzen & Solomon, 1980; Sinnhuber et al., 2012; Solomon et al., 1981, 1983; Verronen et al., 2006, 2007, Weeks et al., 1972). Based on March 2005 and April 2006 as case studies, Verronen et al. (2011) found that 56–87% of the OH variation at 71- to 78-km altitudes can be explained by EEP. The time period of 1 month considered is rather short and will as such not reflect the general situation. Considering the period 2004–2009, Andersson et al. (2012) found a strong correlation of $r \geq 0.6$ (or $r^2 \geq 36\%$) between OH and 100- to 300-keV precipitating electrons at 70- to 78-km altitude. Although simple correlation analyses show high correlation between OH and precipitating electrons, this correlation will also be affected by OH variability from other sources, for example, photolysis of H_2O or planetary wave activity (Zawedde et al., 2016). The magnitude of this correlation may significantly change if the various probable sources of OH variability are taken into account (i.e., when other variables are held constant).

The mesospheric OH response to energetic electron energy deposition has been modeled on different time scales, for different types of events and for different geographic locations in the atmosphere (see, e.g., Aikin & Smith, 1999; Turunen et al., 2016; Verronen et al., 2013, 2015). Daae et al. (2012), Verronen et al. (2013), and Andersson, Verronen, Rodger, Clilverd, and Seppälä (2014) have discussed whether the frequent EEP events could have an impact on mesospheric OH comparable to the impact due to the infrequent SPEs over long time scales. The recurrent geomagnetic activity associated with EEP is known to vary strongly throughout a given solar cycle and will produce a continuous and significantly fluctuating source of variability in mesospheric constituents. Therefore, they suspect that on solar cycle time scales, the EEP forcing could be more important to mesospheric OH and ozone (O_3) than SPEs. Andersson, Verronen, Rodger, Clilverd, and Seppälä (2014) show that on solar cycle time scales, the direct HO_X-driven effect due to EEP causes significant variability in mesospheric O_3. They, therefore, suspect that EEP could be an important contributor to Sun-climate connection on solar cycle time scales.

In a recent study, Zawedde et al. (2016) show that during solar minimum, EEP-driven OH production is comparable with OH production due to the background atmospheric dynamics. Since EEP events are generally weak,

their contribution to OH variability may be masked by the seasonal trend in H_2O and solar Lyman-α radiation and shorter term variations such as SSWs. This may also depend on the altitude and the geographical location. Therefore, to quantify the EPP effect, the background atmospheric dynamics, along with detailed knowledge of where and when the precipitation occurs, needs to be taken into account. This, however, requires a method that can simultaneously take into consideration all the available sources of OH variability. This method should be able to consider the day-to-day variability in OH due to H_2O and Ly-α radiation as well as other atmospheric parameters, for example, temperature that capture the daily and seasonal variability. In addition, the contribution from energetic particles should also be accounted for. One way to achieve this goal is by using multiple linear regression to assess the contribution from a parameter when all the other parameters are held constant.

By applying a new analysis technique on measurements from the Medium Energy Proton and Electron Detector (MEPED) on the National Oceanic and Atmospheric Administration (NOAA) Polar Orbiting Environmental Satellites (POES), an estimate of the flux of precipitating electrons is obtained by measurements from both the 0° and 90° telescopes (Nesse Tyssøy et al., 2016; Ødegaard et al., 2017). An estimate of the flux of precipitating protons is obtained by combining measurements from the MEPED 0° telescope and the omnidirectional detectors (0–60°) (Nesse Tyssøy et al., 2013; Nesse Tyssøy & Stadsnes, 2015). The known challenges with NOAA POES data (see, e.g., Evans & Greer, 2000; Ødegaard et al., 2017; Sandanger et al., 2015; Yando et al., 2011) are overcome, giving a realistic estimate of the precipitating fluxes throughout the mesosphere.

It is from this perspective that we draw the objectives for this study. We use multiple linear regression to model the natural atmospheric background variability of OH in order to estimate and understand the impact of EPP on OH in general in both a geographic and magnetic coordinate system. We further investigate the relative importance of SPEs and EEP during the declining phase of solar cycle 23 (2005–2009). We analyze OH, temperature, geopotential height (GPH), and H_2O observations from the MLS instrument on board the Aura satellite and particle data from the NOAA POES satellites for the years 2005–2009. Composite solar Ly-α radiation from the Thermosphere Ionosphere Mesosphere Energetics and Dynamics (TIMED) and the Solar Radiation and Climate Experiment (SORCE) spacecrafts is also included in the analysis. In the following study, we investigate and discuss the relative contribution to OH variability from the background parameters and the solar energetic particles during the years 2005–2009.

2. Data

2.1. NOAA POES MEPED Observations

The NOAA/POES satellites provide an extensive data set of particle fluxes as measured by the MEPED 0° and 90° telescopes which are part of the Space Environment Monitor-2 instruments on board these satellites. We use particle data from NOAA-16 for year 2005 and NOAA-18 particle data for the years 2006 to 2009. The NOAA-16 and NOAA-18 particle measurements are closest in time and space to the atmospheric observations by the Aura MLS satellite.

The two MEPED electron solid-state detectors monitor the intensity of electrons in three nominal energy bands: >30, >100, and >300 keV (Evans & Greer, 2000), whose known data challenges have been catered for using the new analysis toolbox described by Nesse Tyssøy et al. (2016). In this toolbox, the proton fluxes are corrected for degradation due to radiation damage by applying correction factors derived by Sandanger et al. (2015) and Ødegaard et al. (2016). The corrected proton data are then used to correct the electron data from proton contamination. Since the geometric factor for the electron detectors varies with energy, Ødegaard et al. (2017) calculated new optimized geometric factors and the associated new energy thresholds for the electron channels are >43, >114, >292, and >757 keV. The fourth electron channel is derived from relativistic electron contamination of the p6 channel of the proton telescope detectors as described by Nesse Tyssøy et al. (2016).

If there is strong pitch angle diffusion and an isotropic distribution of the particles, the 0° and 90° telescopes give a realistic estimate of the precipitating particle fluxes. Otherwise the 0° and 90° telescopes will either underestimate or overestimate the flux of the precipitating particles, respectively, with decreasing fluxes toward the center of the loss cone (Nesse Tyssøy et al., 2016; Rodger et al., 2010, 2013). Therefore, a complete bounce loss cone flux is constructed for each of the new electron energy channels (Ødegaard et al., 2017), using measurements from both the 0° and 90° telescopes in conjunction with electron pitch angle distribution theory as described by Nesse Tyssøy et al. (2016). We convert the integral fluxes into a differential

electron spectrum covering energies from 43 to 757 keV, which in turn is used to calculate the energy deposition as a function of altitude. In these calculations, we use the cosine-dependent Isotropic over the Downward Hemisphere model of Rees (1989). This is a range-energy analysis based on a standard reference atmosphere (COmmittee on SPAce Research, International Reference Atmosphere 1986).

To monitor the strong solar proton precipitation, we combine the measurements from MEPED proton telescope (0°) with measurements from the MEPED omnidirectional detector system (0–60°) as described in Nesse Tyssøy et al. (2013) and Nesse Tyssøy and Stadsnes (2015). The proton telescope measures the proton fluxes in six energy bands over the range >30 to >6,900 keV, while the omnidirectional telescope measures the proton fluxes with energies >16 to >70 MeV. At high latitudes, both the 0° detector and the omnidetector measure protons in the loss cone. Under the assumption of isotropic fluxes, which is expected during SPEs, we combine the measurements from the two detector systems to obtain integral spectra by fitting monotonic piecewise cubic Hermite interpolating polynomials (Fritsch & Carlson, 1980) to the measurements. The energy deposition height profile for protons is calculated based on range energy of protons in air given by Bethe and Ashkin (1953). The atmospheric densities are retrieved from the MSIS-E-90 model (Hedin, 1991). We include the SPEs (>1,000 particle flux units) from 2005 to 2009 presented in Nesse Tyssøy and Stadsnes (2015).

2.2. Aura MLS Observations

The Aura satellite is one of the three Earth Observing System/National Aeronautics and Space Administration core platforms (Schoeberl et al., 2006). Launched in 2004, the Aura satellite focuses on observing atmospheric composition and it is dedicated to understanding the changing chemistry of our atmosphere. It is in a near polar sun-synchronous orbit at 705-km altitude, giving daily global coverage with about 14 orbits per day. The MLS is one of the four instruments on board Aura. Aura MLS measures naturally occurring microwave thermal emissions from the limb of Earth's atmosphere to remotely sense vertical profiles of atmospheric constituents, every 25 s (Schoeberl et al., 2006; Waters et al., 2006).

In this study, we use Aura/MLS Level 2 files version 4.2x data for the years 2005 to 2009. We use Northern Hemisphere (NH) nighttime data which are screened following the instructions in the data quality and description document (Livesey et al., 2015). The OH sensitivity to changes in temperature and H_2O is modest during nighttime compared to daytime, indicating a better possibility of identifying EEP effects on OH at night (Andersson et al., 2012). For the NH, considering the SZA >100° selection, approximately 97% of the MLS observations occur at solar local times 2–5 in the geographic latitude band of 45–80°N. When a corrected geomagnetic (CGM) latitude band of 55–70°N is considered, the SZA >100° selection gives solar local times 2–4. The temporal, vertical, and horizontal resolution of OH are 25 s, 2.5 km, and 165 km, respectively, within mesospheric altitudes (60–80 km). The vertical and horizontal resolutions of temperature, GPH, and H_2O are variable and coarser within the mesosphere (see Livesey et al., 2015). The pressure levels are converted into geometric height.

The local oscillator signal driving the Aura MLS 2.5-THz radiometers (from which OH measurements are derived) is provided by a methanol laser which in December 2009 began to show signs of aging and was temporarily deactivated (Livesey et al., 2015). In order to conserve the remaining lifetime of the THz instrument for valuable measurements when the Sun becomes more active, OH measurements were suspended from December 2009 to August 2011.

2.3. Solar Lyman-Alpha

The time series for the daily composite solar Ly-α radiation are retrieved from the Laboratory for Atmospheric and Space Physics Interactive Solar IRradiance Datacenter. For the years 2005–2009, the composite Ly-α times series consist of irradiance measurements from the Solar Extreme ultraviolet Experiment and the Solar Stellar Irradiance Composition Experiment instruments on board the National Aeronautics and Space Adminsitration's TIMED and SORCE spacecrafts respectively.

Since the amount of solar radiation at a certain altitude varies as a function of the SZA, applying the exponential function of the secant of the SZA to the daily composite solar Ly-α radiation yields a function of the form (see Andersson et al., 2012):

$$I_{\alpha}^{\mathrm{SZA}} = I_{\alpha}\exp[-\beta\sec(\mathrm{SZA}_{\mathrm{min}})] \quad (2)$$

where β is a an altitude dependent fit parameter related to the optical depths of ultraviolet absorption by O_3 and molecular oxygen (O_2), SZA_{min} is the daily minimum SZA for which the intensity of solar ultraviolet radiation is maximum and I_α is the daily composite solar Ly-α radiation (approximately the Ly-α radiation at the top of the atmosphere). Assuming β to be unity gives the general daily variation in solar Ly-α radiation with SZA.

3. Methods and Results

3.1. Variation of OH

Figure 1 (top to bottom) shows the daily mean temperature, H_2O, GPH, I_α^{SZA}, electron energy deposition, proton energy deposition (for SPEs periods), and OH for years 2005 to 2009 averaged over a geographic (GEO) latitude band of 45–80° (left) and a CGM latitude band of 55–70° (right) in the NH. All averages are for 78-km altitude during nighttime except I_α^{SZA} which shows variation when β is unity during daytime. This is the case because we are only interested in the change in I_α^{SZA} and not the optical properties (optical depth) of the atmosphere which vary with altitude.

The temperature, H_2O, GPH, and I_α^{SZA} (top two panels) exhibit a strong seasonal periodic dependence for both geographic (left) and CGM (right) latitudinal averages. The seasonal behavior is such that high values of GPH, H_2O, and I_α^{SZA} correspond to low values of the temperature at 78-km altitude during summer, whereas low values of GPH, H_2O, and I_α^{SZA} are associated with high temperatures during winter. The electron energy deposition (third panels) shows a continuous signature, whereas protons show four distinct peaks for both geographic and CGM averages. Averaging over the geographic latitude band gives a strong signal of the proton energy deposition while weakening the signature from the electrons as the electrons are only deposited in a relatively small band within the geographic latitude band. Averaging over the CGM latitude range of the radiation belts covers most of the electron energy deposition resulting in a strong signature of electrons while that of the protons is less prominent as the SPEs protons will be cut off depending on their rigidity (Nesse Tyssøy & Stadsnes, 2015). As such, it is important to investigate both kinds of averages since the electrons and protons exert a somewhat different forcing in the two different latitude band averages.

The OH daily means also exhibit a seasonal variation but not as smooth and periodic as the temperature, H_2O, GPH, and I_α^{SZA}. There are distinct strong peaks in the OH daily means corresponding to the peaks in the proton energy deposition for OH averaged over the geographical latitude band. Peaks in OH corresponding to the electron energy deposition are, however, not that evident. When OH is averaged over the latitude range of the radiation belts (CGM 55–70°N), the data exhibit stronger short-term variability; hence, it is quite difficult to isolate the OH peaks that are attributed to protons as well as those due to electrons. Apart from the narrow distinct peaks associated with SPEs, OH also exhibits other relatively broader peaks during some of the winters (2006, 2007, and 2009) associated with SSWs, shown by the vertical dashed lines. For a comprehensive list of SSWs during the years 2005 to 2009 see, for example, Damiani et al. (2010). The narrow peaks associated with SPEs weaken for averages over the CGM latitude band, but the broad winter SSWs OH peaks seem to persist in both the geographic and CGM latitudinal averages.

3.2. Regression Analysis

The data are sorted by geographic coordinates; 45–80°N and by CGM coordinates; 55–70°N. Then daily averages are calculated for the respective altitudes. Triangulation-based linear interpolation is used to obtain temperature, GPH, and H_2O data at altitudes at which Aura MLS does not retrieve observations. To allow for normality of the regression models residuals, OH is transformed by taking its logarithm for all regression analyses. A constant is added to OH to ensure that the logarithms are all real.

To reduce structural collinearity, the predictors are centered by subtracting the mean from the predictor variables. Structural collinearity results from inclusion of higher-order terms like interactions and squares into the regression model. Hence, centered variables are used in the following multiple regression analysis and for the simple regression for consistency.

The adjusted R^2 (also known as the adjusted coefficient of determination) gives a measure of how much of the variation in the dependent (response) variable is explained by the regression model. The adjusted R^2 is used throughout to determine how good the models fit the observed OH at a particular altitude.

Figure 2 shows the regression workflow hereafter followed through out the methods and results. The magenta, brown, and orange arrows represent the pathways for simple linear regression, multiple linear

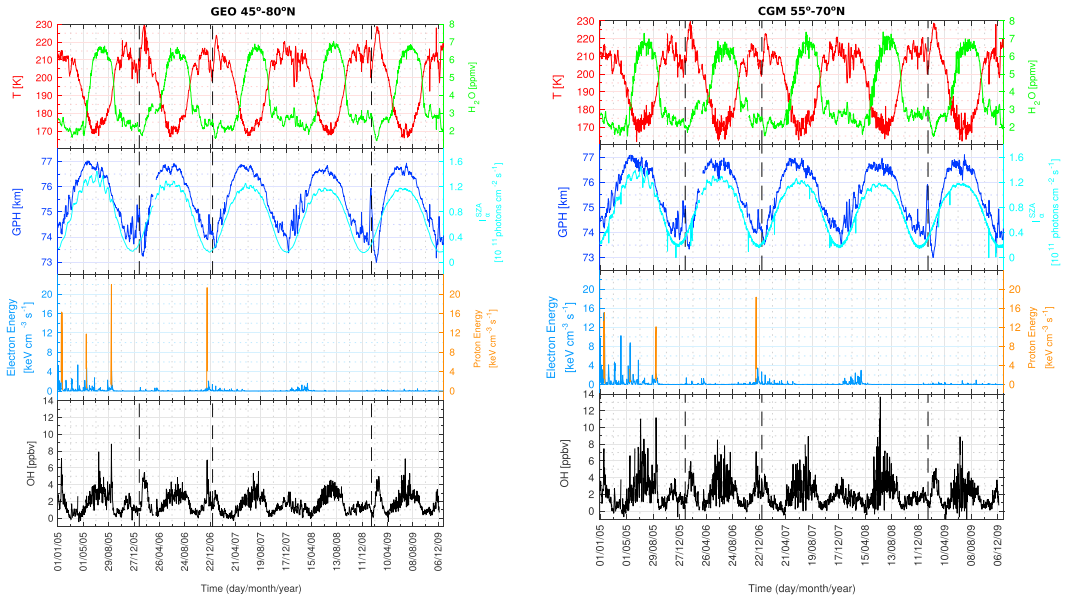

Figure 1. General view of the variation of the nighttime daily mean temperature, geopotential height (GPH), H_2O, I_α^{SZA}, energy deposition (electrons and protons), and hydroxyl (OH) during the years 2005 to 2009 averaged over a geographic latitude band of 45–80°N (left) and a corrected geomagnetic latitude band of 55–70°N (right). The temperature, GPH, H_2O, energy deposition (electrons and protons), and OH are daily averages at 78 km. Whereas I_α^{SZA} is for $\beta = 1$ (neglecting the altitude dependence in β). The vertical dashed lines denote some of the sudden stratospheric warmings for illustration.

regression for the background, and multiple linear regression of the background plus the particle energy deposition, respectively.

3.2.1. Simple Linear Regression

The top panels in Figure 3 show the Pearson's correlation performed on the OH and the proposed predictor variables: temperature, GPH, H_2O, and I_α^{SZA} separately for the years 2005 to 2009. The correlation is deemed significant for p values < 0.05 (95% confidence interval). There exists a significant correlation between OH and the proposed predictors; temperature, GPH, H_2O, and I_α^{SZA} for all altitudes except at 62 and 67 km for GPH and I_α^{SZA}. The single strongest correlation is found at 75 km followed by 78 km between OH and temperature, and OH and H_2O respectively in both the geographic and CGM framework.

Given the predictors variables; temperature, GPH, H_2O, and I_α^{SZA}, a simple linear regression model for the OH time series is given by:

$$OH(t) = C_0 + C_1 X(t) + \epsilon(t), \qquad X = T, GPH, H_2O, I_\alpha^{SZA} \tag{3}$$

where ϵ represents the random errors (or residuals) which must be normally distributed independent random variables with mean zero and constant variance (see Rawlings et al., 1998). The regression coefficients, C_0 and C_1, are listed in Table 1. For both kinds of coordinate averages, simple linear regression captures the general seasonal trend in the OH variability but fails to capture the variations due to SSWs. In order to estimate the EPP impact over the declining phase of solar cycle 23, the regression analysis must capture both long-term seasonal variation as well as short-term variability. Nevertheless, simple linear regression with H_2O gives a consistently high adjusted R^2 (>10%) for altitudes 64, 67, 73, 75, and 78 km in a geographic setting (Table 1). In a CGM setting, both temperature and H_2O give high adjusted R^2 for altitudes 73–78 km. The level of variation in OH explained by the simple linear regression models is relatively low for altitudes below 73 km.

To account for nonlinear effects in the predictors: temperature, GPH, H_2O, and I_α^{SZA}, second-order polynomial (or quadratic) regression is opted for. But in order to adhere to the *hierarchy principle*, all lower order terms are included in the model whether or not the coefficients for these effects are significant. Therefore, the second-order polynomial regression model of the response variable OH and with any of the predictor variables X is given by:

$$OH(t) = C_0 + C_{11} X(t) + C_{12} X^2(t) + \epsilon(t), \qquad X = T, GPH, H_2O, I_\alpha^{SZA} \tag{4}$$

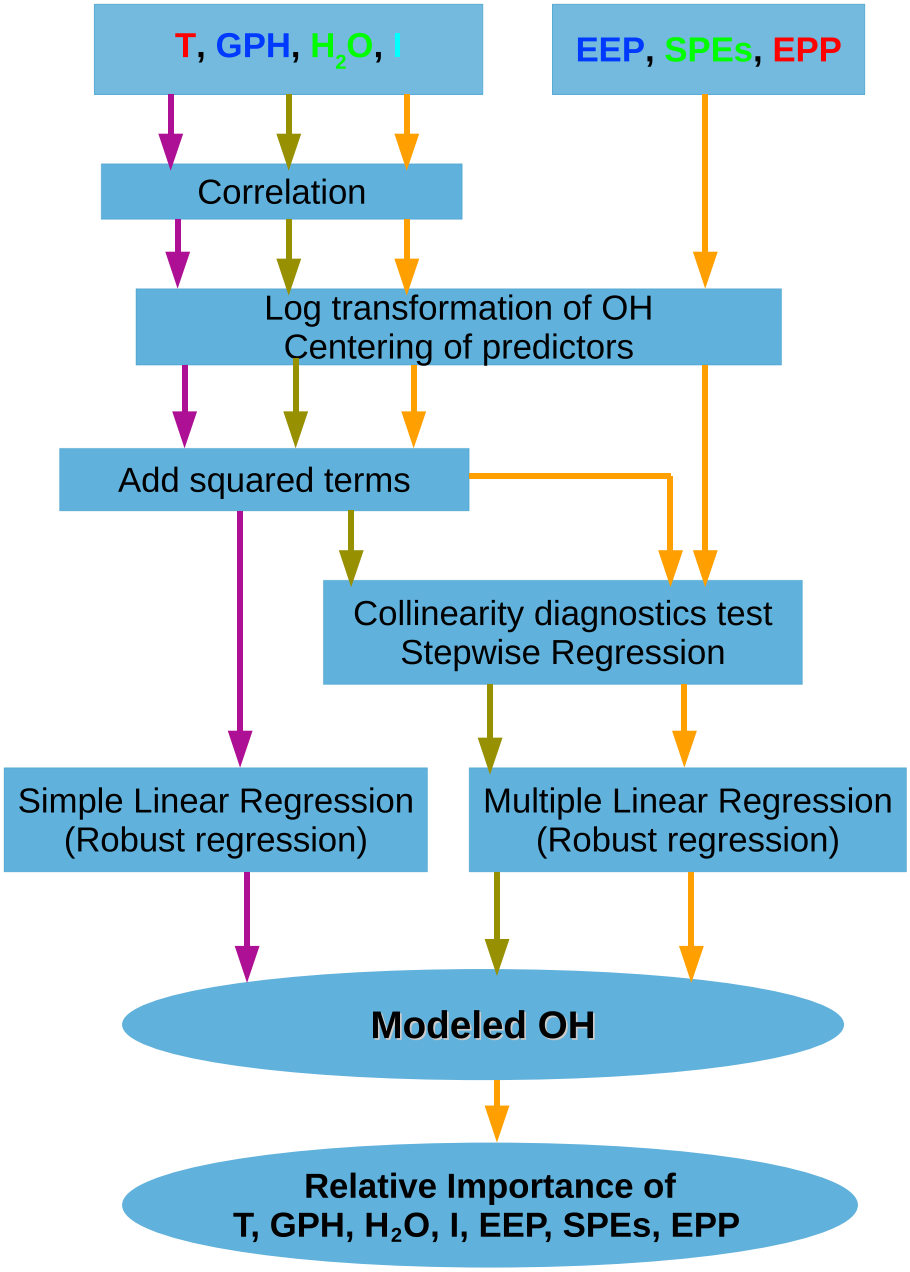

Figure 2. A flow diagram showing a summary of the workflow of methods used for linear regression analyses in this paper. The magenta arrows represent the pathway for simple linear regression. The Brown arrows represent the pathways for multiple linear regression for background hydroxyl (OH) variability. The Orange arrows represent the flowlines for multiple linear regression of the background OH variability plus the particle energy deposition. The variables OH, T, GPH, H_2O and I are: hydroxyl, temperature, geopotential height, water vapor and solar Lyman alpha radiation, respectively. The acronyms EPP, SPEs and EEP represent: energetic particle precipitation, solar proton events and energetic electron precipitation, respectively.

where C_0, C_{11}, and C_{12} are the regression coefficients also listed in Table 2 and ϵ represents the error term to account for the discrepancy between the predicted and observed response variable. Simple quadratic regression not only accounts for the nonlinear effects in the predictors but also improves the amount of variation explained by the regression models especially for altitudes above 70 km (see Figure 4a).

Temperature seems to explain more variability in OH than any of the other predictors at altitudes 75 and 78 km (see Figure 4a). The time plot of the observed and modeled OH for 2005 to 2009 from quadratic regression with temperature as the only predictor variable is shown in Figure 5. The adjusted R^2 is higher for models

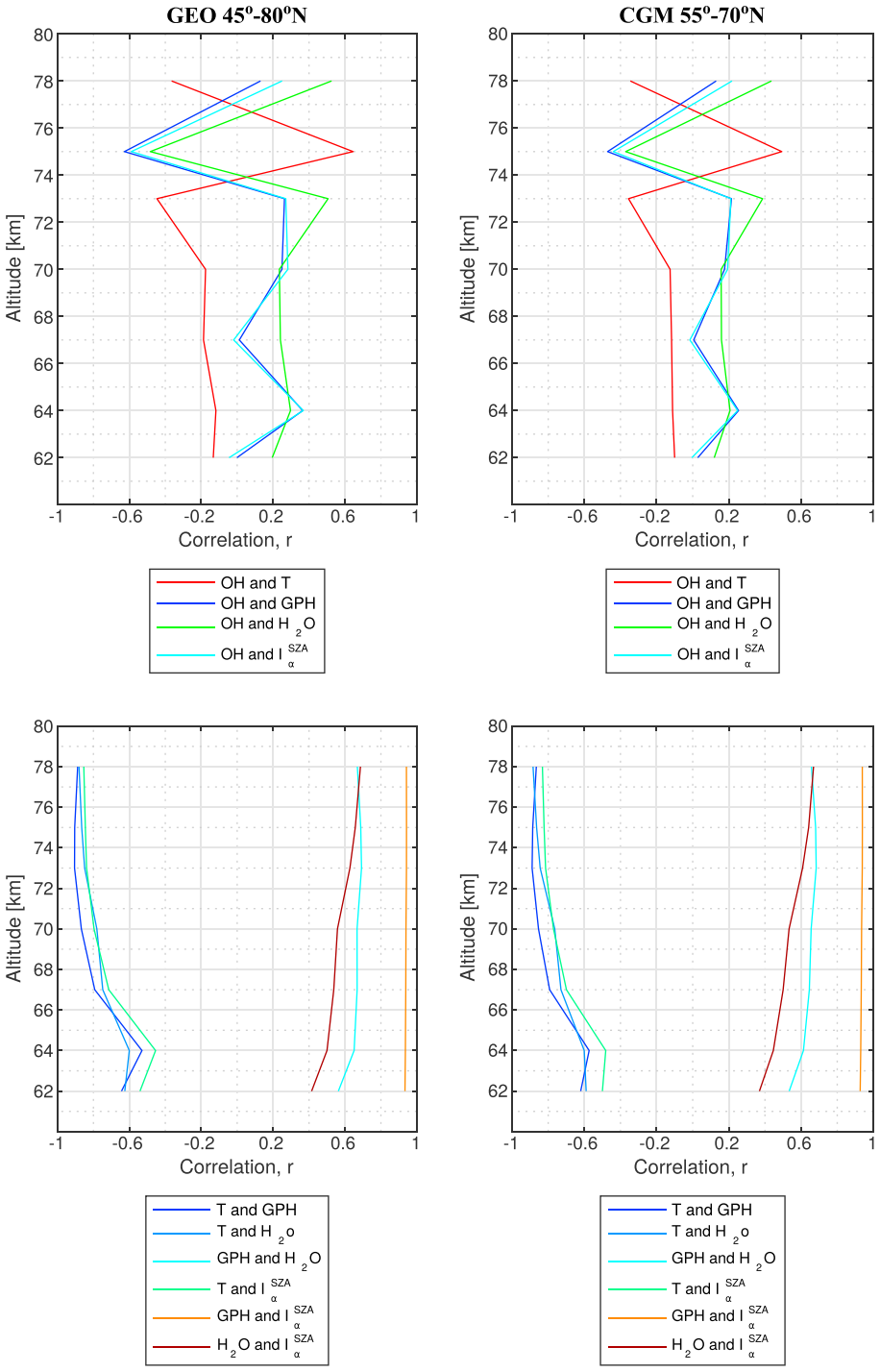

Figure 3. Top: Correlation between daily mean OH and each of the proposed predictor variables: Temperature, GPH, H_2O and I_α^{SZA}. Bottom: Correlation among pairs of predictor variables. The variables OH, GPH, H_2O and I_α^{SZA} are: hydroxyl, geopotential height, water vapor and solar Lyman alpha radiation as a function of the solar zenith angle, respectively. The acronyms GEO and CGM represent: geographic and corrected geomagnetic respectively.

for which the data are averaged over a geographical latitude band than for a CGM latitude band at the same altitude. Note that altitude 75 km displays a rather peculiar behavior in OH variability. For averages over the geographical latitude band, summers exhibit low OH volume mixing ratio (VMR) while winters exhibit high OH VMR at 75-km altitude, which behavior is reflected by the regression models. However, for averages

Table 1
Simple Linear Regression: Linear Regression Coefficients for Years 2005 to 2009 for a Geographic Latitude Band of 45–80°N (Left) and a CGM Latitude Band of 55–70°N (Right)

	Alt	GEO			CGM		
Var	(km)	C_0	C_1 (10^{-4})	R^2	C_0	C_1 (10^{-4})	R^2
	78	0.74	−22.88	**0.24**	0.76	−19.60	**0.12**
	75	0.56	21.93	**0.55**	0.56	26.48	**0.49**
	73	0.65	−8.94	**0.31**	0.66	−8.42	**0.18**
T	**70**	0.60	−1.67	**0.04**	0.60	−0.45	**0.03**
	67	0.61	−1.93	**0.09**	0.61	−1.35	**0.03**
	64	0.60	−0.77	**0.05**	0.60	−0.47	**0.08**
	62	0.60	−0.33	**0.02**	0.60	−0.27	**0.02**
	78	0.75	135.58	**0.03**	0.76	68.29	**0.01**
	75	0.56	−273.19	**0.46**	0.56	−317.14	**0.38**
	73	0.65	58.54	**0.11**	0.65	45.35	**0.06**
GPH	**70**	0.60	23.36	**0.11**	0.60	16.88	**0.05**
	67	0.61	1.21	**0.02**	0.61	−2.67	**0.02**
	64	0.60	11.01	**0.27**	0.60	10.49	**0.16**
	62	0.60	−0.52	**0.01**	0.60	−1.51	**0.03**
	78	0.74	300.80	**0.43**	0.76	255.21	**0.20**
	75	0.56	−172.07	**0.31**	0.57	−194.20	**0.24**
	73	0.65	93.62	**0.36**	0.66	84.59	**0.20**
H_2O	**70**	0.60	20.78	**0.08**	0.60	15.57	**0.05**
	67	0.61	14.50	**0.11**	0.61	11.57	**0.04**
	64	0.60	10.94	**0.14**	0.60	8.53	**0.10**
	62	0.60	4.55	**0.04**	0.60	3.99	**0.02**
	78	0.75	578.22	**0.07**	0.76	416.69	**0.03**
	75	0.56	−814.53	**0.40**	0.56	−954.29	**0.32**
	73	0.65	206.74	**0.11**	0.65	155.51	**0.05**
I_α^{SZA}	**70**	0.60	103.05	**0.14**	0.60	81.33	**0.07**
	67	0.61	−3.96	**0.03**	0.61	−22.47	**0.04**
	64	0.60	46.58	**0.26**	0.60	43.64	**0.15**
	62	0.60	−5.78	**0.03**	0.60	−12.16	**0.06**

Note. The response variable is $\log_{10}(\mathrm{OH} + \text{constant})$. The constant (4) is added to ensure only positive values of OH and hence only real logarithms of OH. The predictor variables are temperature, GPH, H_2O, and I_α^{SZA}. The coefficient of determination is given by the adjusted R^2. The variables OH, GPH, H_2O and I_α^{SZA} are: hydroxyl, geopotential height, water vapor and solar Lyman alpha radiation as a function of the solar zenith angle, respectively. The acronyms GEO and CGM represent: geographic and corrected geomagnetic, respectively.

over the CGM latitude band, summers exhibit some rather high variability in OH that are not reflected by the regression models. A summary of the simple linear regression workflow is shown in Figure 2 by the magenta arrows.

3.2.2. Multiple Linear Regression

Correlation between a predictor and OH may not necessarily imply causality. We wish to combine the regression analysis with all the different parameters to allow for detection of the contribution from each predictor variable when other variables are held constant. Therefore, the OH background multiple second-order polynomial regression equation for a pure quadratic model (without interaction terms) with predictors temperature, GPH, H_2O and I_α^{SZA} is of the form:

$$\mathrm{OH}(t) = C_0 + C_{j1}T(t) + C_{j2}T^2(t) + C_{k1}G(t) + C_{k2}G^2(t) + C_{l1}H(t) + C_{l2}H^2(t) + C_{m1}I(t) + C_{m2}I^2(t) + \epsilon(t) \quad (5)$$

Table 2
Simple Linear Regression: Second-Order Polynomial (Quadratic) Regression Model Coefficients for Years 2005 to 2009 for a Geographic Latitude Band of 45–80° N (Left) and a CGM Latitude Band of 55–70° N (Right)

	Alt	GEO				CGM			
Var	(km)	C_0	C_{11} (10^{-4})	C_{12} (10^{-4})	R^2	C_0	C_{11} (10^{-4})	C_{12} (10^{-4})	R^2
	78	0.68	−8.33	2.28	**0.56**	0.69	−7.81	2.39	**0.45**
	75	0.56	22.17	0.16	**0.54**	0.56	26.49	−0.03	**0.49**
	73	0.65	−8.05	0.40	**0.39**	0.65	−8.37	0.34	**0.26**
T	**70**	0.60	−2.04	0.21	**0.10**	0.60	−0.92	0.16	**0.06**
	67	0.61	−2.60	0.18	**0.14**	0.61	−1.78	0.10	**0.04**
	64	0.60	−0.32	−0.12	**0.08**	0.60	−0.09	−0.09	**0.09**
	62	0.60	−0.65	0.06	**0.06**	0.60	−0.70	0.07	**0.05**
	78	0.70	243.65	424.11	**0.24**	0.71	189.11	449.79	**0.18**
	75	0.57	−288.28	−50.80	**0.49**	0.57	−344.26	−72.78	**0.42**
	73	0.64	68.22	46.09	**0.20**	0.65	60.87	47.22	**0.11**
GPH	**70**	0.60	26.82	12.12	**0.15**	0.60	19.27	5.53	**0.06**
	67	0.61	1.70	1.49	**0.02**	0.61	−2.59	0.16	**0.02**
	64	0.60	11.87	2.00	**0.29**	0.60	11.46	1.45	**0.17**
	62	0.60	0.36	1.81	**0.05**	0.60	−0.04	1.97	**0.03**
	78	0.71	172.45	113.32	**0.46**	0.72	119.10	127.41	**0.25**
	75	0.58	−140.51	−47.08	**0.35**	0.58	−142.06	−68.36	**0.30**
	73	0.64	68.25	50.07	**0.50**	0.64	63.42	48.38	**0.31**
H_2O	**70**	0.60	20.80	−0.15	**0.08**	0.60	15.58	0.05	**0.05**
	67	0.61	15.14	7.14	**0.15**	0.61	12.12	3.58	**0.05**
	64	0.60	11.90	3.45	**0.17**	0.60	9.80	2.79	**0.12**
	62	0.60	4.96	1.53	**0.04**	0.60	3.94	−0.14	**0.02**
	78	0.70	892.30	2,981.60	**0.24**	0.71	819.08	3,509.60	**0.18**
	75	0.57	−885.15	−604.14	**0.43**	0.57	−1,057.70	−680.53	**0.36**
	73	0.65	251.49	480.36	**0.17**	0.65	211.37	417.30	**0.08**
I_α^{SZA}	**70**	0.60	119.46	136.78	**0.16**	0.60	100.83	124.41	**0.08**
	67	0.61	−0.99	25.71	**0.03**	0.61	−21.17	8.37	**0.03**
	64	0.60	54.94	55.76	**0.31**	0.60	56.06	61.13	**0.18**
	62	0.60	−1.27	29.88	**0.04**	0.60	−6.00	29.06	**0.04**

Note. The coefficients C_{11} and C_{12} are associated with the predictor variables temperature, GPH, H_2O, I_α^{SZA} and their squared terms, respectively. The response variable is $\log_{10}(OH + constant)$. The constant (4) is added to ensure only positive values of OH and hence only real logarithms of OH. The coefficient of determination is given by the adjusted R^2. The variables OH, GPH, H_2O and I_α^{SZA} are: hydroxyl, geopotential height, water vapor and solar Lyman alpha radiation as a function of the solar zenith angle, respectively. The acronyms GEO and CGM represent: geographic and corrected geomagnetic, respectively.

where C_0, C_{j1}, C_{j2} … C_{m1}, C_{m2} are the regression coefficients (also listed in Table 3) and ϵ is the error term. Polynomial regression allows for a nonlinear relationship between the response variable and the predictors as well as maintaining a linear regression framework (linear in the regression coefficients). The coefficients for multiple linear regression without quadratic terms are also listed in Table 3 for completeness.

It is, however, evident that there is significant correlation among the predictor variables as shown in Figure 3 (bottom panels), which is strongest between GPH and I_α^{SZA}. The violation of the basic assumptions of normality, independence, and constant variance of the residuals and the predictor variables being measured without error leads to problems in least squares regression analysis (see Rawlings et al., 1998). Correlation among predictor variables, however, does not always result in collinearity. The inclusion or exclusion of a certain predictor for example H_2O may increase or decrease collinearity.

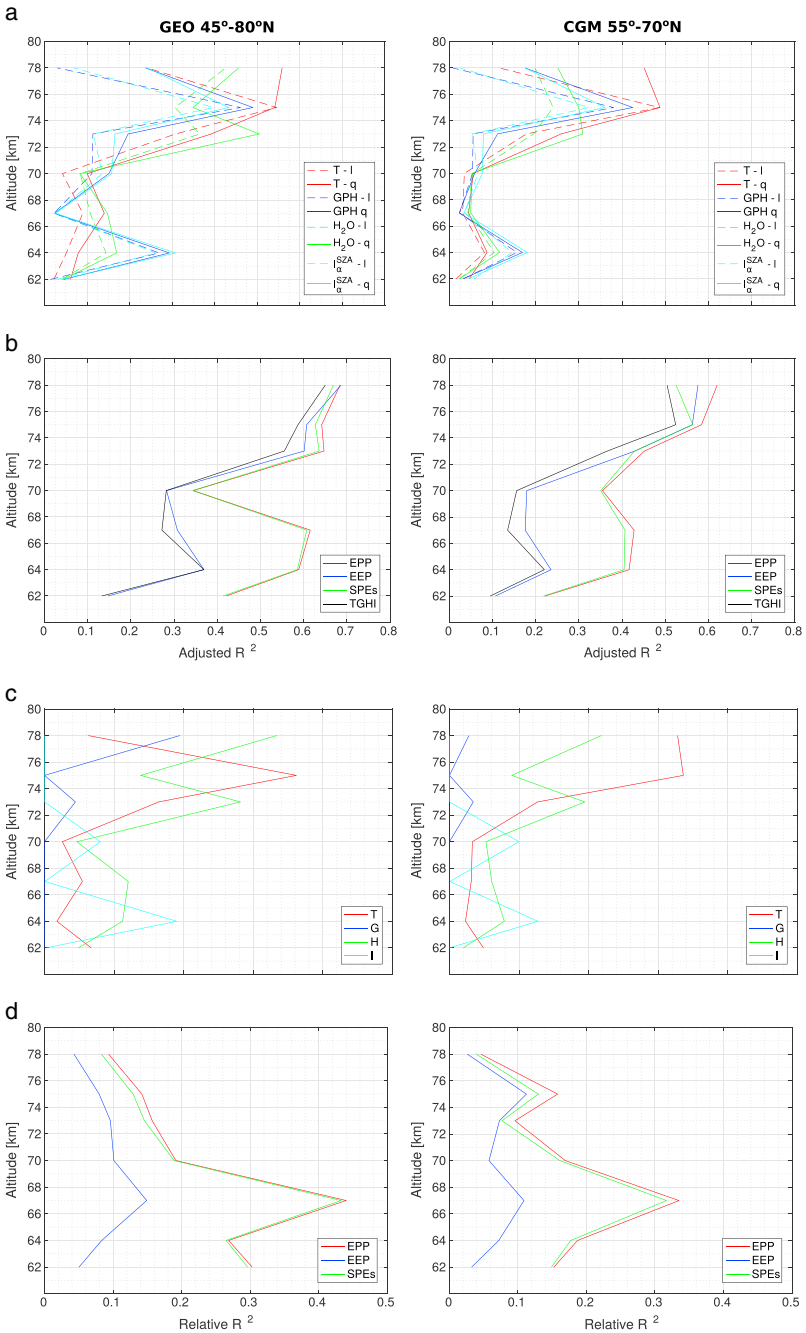

Figure 4. Line plots showing the amount of variation in OH explained by the different regression models for years 2005 to 2009. The data are averaged within the geographical (GEO) latitude range of 45–80°N (left) and within a corrected geomagnetic (CGM) latitude range of 55–70°N (right). (a) Adjusted R^2 from simple linear regression. The dotted lines represent linear (*l*) regression models, whereas the solid lines represent the quadratic (*q*) models. The colors red, blue, green, and cyan represent temperature, GPH, H_2O, and I_α^{SZA}, respectively. (b) Adjusted R^2 from multiple linear regression. The black lines represent the model of the background OH variability. The red lines represent the model of the background plus the energetic particle precipitation (electrons and protons). The blue lines represent the model with only electrons added, while the green lines represent a model for which only protons are added to the background. (c) Relative importance of temperature, GPH, H_2O, and I_α^{SZA} in a model for which the total energy (EPP) is added. (d) Relative importance of EEP, SPEs, and EPP shown by the amount variation explained by each kind of forcing at a particular altitude.

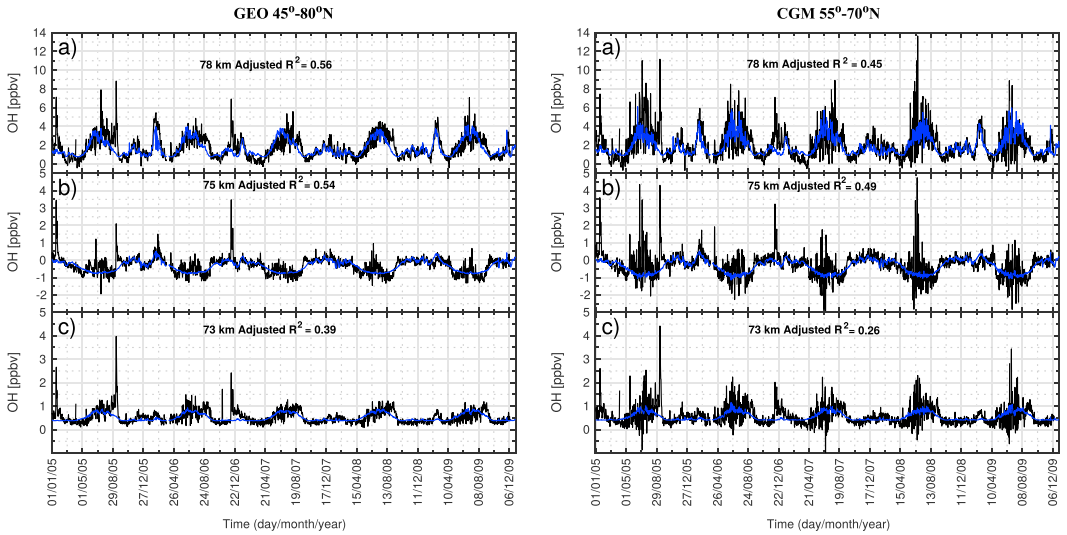

Figure 5. Simple Linear Regression: Second-order polynomial regression of the response variable hydroxyl (OH) and temperature as the predictor for years 2005–2009. The data are averaged within the geographic (GEO) latitude range of 45–80°N (left) and a corrected geomagnetic (CGM) latitude band of 55–70° N for altitudes 73, 75, and 78 km. The black line represents the OH observation, while the blue line represents the modeled OH.

Therefore, we performed Belsley et al. (2005) collinearity diagnostics that assesses the sources and the associated strength of collinearity among variables using condition indices and variance decomposition. The condition indices identify the number and strength of any near dependencies in the predictor variables. Whereas the variance-decomposition proportions identify groups of predictors involved in near dependencies, and the extent to which the dependencies may degrade the regression coefficients. The predictor terms for which the condition index is >10 and the variance decomposition is > 0.5 are deemed to degrade the regression coefficients and are therefore excluded from the regression models.

Stepwise regression is used for variable selection. Stepwise algorithm searches for and adds or removes terms until no terms can be added or removed from the model. Using the sum of squared error criterion, the stepwise algorithm adds the terms to the model if the sum of squared error of the model is smaller than 0.05 and removes terms from the model if p value of the F statistic is larger than 0.1. After finding the models' form and the relevant parameters (or terms) using stepwise regression, robust weighted least squares regression with bisquare fitting weight function was used to create models that are least affected by outliers. The models were further tested with both a quadratic (with interaction terms) and a pure quadratic (without interaction terms) models. In the following analysis we show only pure quadratic models as they were less affected by collinearity effects.

As already noted, polynomial regression (q) gives higher adjusted R^2 than linear regression for the same altitude (see, e.g., Figure 4a: the solid lines [q] against the dotted lines [l]). The multiple linear regression model further improves the description of the background variability as illustrated by the solid black lines in Figure 4b. The regression workflow for obtaining the background OH models is summarized in Figure 2 by following the brown arrows. With the background model obtained, then the different types of particle energy deposition are added to the model separately. This results in three models; a model of the background plus the electron energy deposition (EEP), a model of the background plus the proton energy deposition (SPEs), and a model of background plus the total particle energy deposition (EPP) whose coefficients are recorded in Table 4. Figure 6 shows time plots of observed (black line) and modeled OH for years 2005 to 2009 for altitudes 62 km to 78 km in the NH for the geographic latitude band. The same plots but for the CGM latitude band are shown in Figure 7. In blue are the models for the background OH variability, whereas red shows models for which the total energy deposition is included. The altitudes 75–78 km exhibit the highest adjusted R^2 for all models in the geographic and CGM latitudinal settings, respectively. Models under a geographic latitude setting give higher adjusted R^2 than their CGM latitude setting counterparts. The line plots of the adjusted R^2 from the four models is shown in Figure 4b. For the geographical latitude setting, the electron (blue) contribution to the adjusted R^2 is lower than that of the protons (green) at all altitudes except at 78 km.

Journal of Geophysical Research: Space Physics

10.1029/2017JA025038

Table 3

Multiple Linear Regression: Regression Coefficients for Linear (l) and Quadratic (q) Multiple Regression for Years 2005–2009 for a Geographic Latitude Band of 45–80° N (Left) and a CGM Latitude Band of 55–70° N (Right)

		GEO										CGM									
	Alt (km)	C_0	C_{j1} (10^{-4})	C_{k1} (10^{-4})	C_{l1} 10^{-4})	C_{m1} (10^{-4})	C_{j2} (10^{-4})	C_{k2} (10^{-4})	C_{l2} (10^{-4})	C_{m2} (10^{-4})	R^2	C_0	C_{j1} (10^{-4})	C_{k1} (10^{-4})	C_{l1} (10^{-4})	C_{m1} (10^{-4})	C_{j2} (10^{-4})	C_{k2} (10^{-4})	C_{l2} (10^{-4})	C_{m2} (10^{-4})	R^2
	78	0.74	−28.13	−479.43	238.25						**0.48**	0.76	−34.86	−1028.70	159.77	1319.80					**0.31**
	75	0.56	26.81		79.69	−80.22					**0.56**	0.56	29.10		75.90	−201.66					**0.51**
	73	0.65	−16.95	−192.89	36.70	216.21					**0.46**	0.66	−15.55	−173.95	36.23	181.86					**0.28**
l	**70**	0.60	6.07		32.70	181.76					**0.25**	0.60	6.17		32.23	156.26					**0.14**
	67	0.61	−3.30	−14.97	13.49	−21.24					**0.23**	0.61	−2.76	−13.57	12.09	−33.60					**0.11**
	64	0.60	1.36		8.92	45.58					**0.35**	0.60	1.29		8.59	45.49					**0.19**
	62	0.60	−0.36		4.96	−14.04					**0.10**	0.60	−0.34		4.06	−18.23					**0.08**
	78	0.68	17.91	48.53	351.42		1.21	236.46			**0.65**	0.69	0.81	−125.82	234.82		1.52	211.38			**0.50**
	75	0.57	27.98		96.10				−34.26		**0.59**	0.57	32.25		99.38				−42.11		**0.52**
	73	0.64	−10.74	−85.35	38.48			12.28	39.80		**0.56**	0.64	−10.02	−88.31	40.91			15.64	40.84		**0.37**
q	**70**	0.60	6.88		32.52	224.76				187.87	**0.28**	0.60	6.92		32.44	203.12				187.72	**0.16**
	67	0.61	−2.44		14.76	−76.02			8.67		**0.27**	0.61	−2.11		13.38	−87.87			7.47		**0.13**
	64	0.60	1.24		8.04	51.32				36.08	**0.37**	0.60	1.21		7.99	55.45				48.80	**0.22**
	62	0.60	−0.55		5.46	−14.37	0.04		3.03		**0.13**	0.60	−0.63		4.71	−18.42	0.04		2.41		**0.09**

Note. The coefficients C_{j1}, …, C_{m1} and C_{j2}, …, C_{m2} are associated with the predictors temperature, GPH, H_2O, I_α^{SZA} and their squared terms, respectively. The response variable is $\log_{10}(\mathrm{OH} + \mathrm{constant})$. The constant 4 is added to ensure that the logarithms of OH are only real. The variables OH, GPH, H_2O and I_α^{SZA} are: hydroxyl, geopotential height, water vapor and solar Lyman alpha radiation as a function of the solar zenith angle, respectively. The acronyms GEO and CGM represent: geographic and corrected geomagnetic, respectively.

Journal of Geophysical Research: Space Physics

10.1029/2017JA025038

Table 4
Multiple Linear Regression: Regression Coefficients for Models That Include the Energy Deposition

		GEO											CGM									
	Alt (km)	C_0	C_{j1} (10^{-4})	C_{k1} (10^{-4})	C_{l1} (10^{-4})	C_{m1} (10^{-4})	C_{n1} (10^{-4})	C_{j2} (10^{-4})	C_{k2} (10^{-4})	C_{l2} (10^{-4})	C_{m2} (10^{-4})	R^2	C_0	C_{j1} (10^{-4})	C_{k1} (10^{-4})	C_{l1} (10^{-4})	C_{m1} (10^{-4})	C_{n1} (10^{-4})	C_{j2} (10^{-4})	C_{k2} (10^{-4})	C_{l2} (10^{-4})	C_{m2} (10^{-4})	R^2
	78	0.69	18.80	37.86	377.47		445.21	1.16	250.19			**0.69**	0.70	2.23	−131.71	270.69		421.28	1.45	238.17			**0.58**
	75	0.57	29.40		115.84		309.35			−37.24		**0.61**	0.57	33.72		121.55		259.53			−48.79		**0.56**
	73	0.64	−10.32	−88.41	46.89		273.48		13.85	38.23		**0.60**	0.64	−9.34	−90.91	51.76		205.16		17.77	39.08		**0.43**
EEP	**70**	0.60	6.89		33.18	223.01	25.34				184.43	**0.28**	0.60	7.13		35.62	195.67	102.41				172.03	**0.18**
	67	0.61	−2.38		15.89	−79.27	172.14			8.99		**0.31**	0.61	−2.00		14.79	−91.08	154.24			7.71		**0.18**
	64	0.60	1.27		8.20	50.45	64.71				34.00	**0.37**	0.60	1.28		8.47	52.64	139.71				42.10	**0.24**
	62	0.60	−0.54		5.76	−15.03	90.55	0.04		3.23		**0.15**	0.60	−0.60		5.16	−19.51	68.65	0.04		2.71		**0.11**
	78	0.69	17.91	45.08	351.64		156.10	1.22	232.05			**0.67**	0.70	0.94	−122.56	236.09		215.81	1.52	208.59			**0.53**
	75	0.57	28.29		97.79		113.30			−33.88		**0.63**	0.57	32.35		99.21		162.88			−41.93		**0.56**
	73	0.64	−10.79	−86.70	38.75		70.74		11.81	40.01		**0.64**	0.64	−9.97	−89.02	41.43		78.50		14.70	41.51		**0.43**
SPE	**70**	0.60	6.86		32.58	222.91	20.01				185.77	**0.34**	0.60	6.88		32.15	200.93	54.25				181.22	**0.35**
	67	0.61	−2.44		14.76	−76.86	28.88			8.73		**0.61**	0.61	−2.10		13.36	−87.02	35.93			7.51		**0.41**
	64	0.60	1.24		7.99	50.71	18.72				35.26	**0.59**	0.60	1.18		7.82	54.25	24.96				45.75	**0.40**
	62	0.60	−0.55		5.50	−14.37	10.62	0.04		3.06		**0.41**	0.60	−0.62		4.61	−18.64	10.86	0.04		2.43		**0.22**
	78	0.69	18.44	45.55	360.98		152.03	1.20	237.13			**0.68**	0.70	1.77	−127.28	259.52		335.30	1.48	230.19			**0.62**
	75	0.57	28.91		106.05		114.71			−34.92		**0.64**	0.57	33.16		112.00		140.38			−45.94		**0.58**
	73	0.64	−10.67	−87.70	40.95		68.44		11.94	39.72		**0.65**	0.64	−9.67	−90.17	45.94		71.92		15.12	41.10		**0.45**
EPP	**70**	0.60	6.88		33.15	221.57	18.89				182.80	**0.34**	0.60	7.01		34.01	196.78	49.36				174.01	**0.35**
	67	0.61	−2.43		14.97	−77.59	28.79			8.82		**0.62**	0.61	−2.08		13.59	−87.50	36.27			7.52		**0.43**
	64	0.60	1.25		8.03	50.41	18.65				34.77	**0.59**	0.60	1.20		7.93	53.98	25.21				45.24	**0.42**
	62	0.60	−0.54		5.51	−14.44	10.71	0.04		3.08		**0.42**	0.60	−0.61		4.67	−18.89	10.83	0.04		2.48		**0.22**

Note. The response variable is $\log_{10}$(OH + constant). The constant 4 is added to ensure that the logarithms of OH are only real. The acronyms EEP, SPE, and EPP stand for the electron, protons and total (electrons plus protons) energy deposition. The coefficients $C_{j1}, \ldots, C_{n1}$ and $C_{j2}, \ldots, C_{m2}$ are associated with the predictors temperature, GPH, H_2O, I_α^{SZA}, energy deposition and the squared terms of temperature, GPH, H_2O, I_α^{SZA}, respectively. The variables OH, GPH, H_2O and I_α^{SZA} are: hydroxyl, geopotential height, water vapor and solar Lyman alpha radiation as a function of the solar zenith angle, respectively. The acronyms GEO and CGM represent: geographic and corrected geomagnetic, respectively.

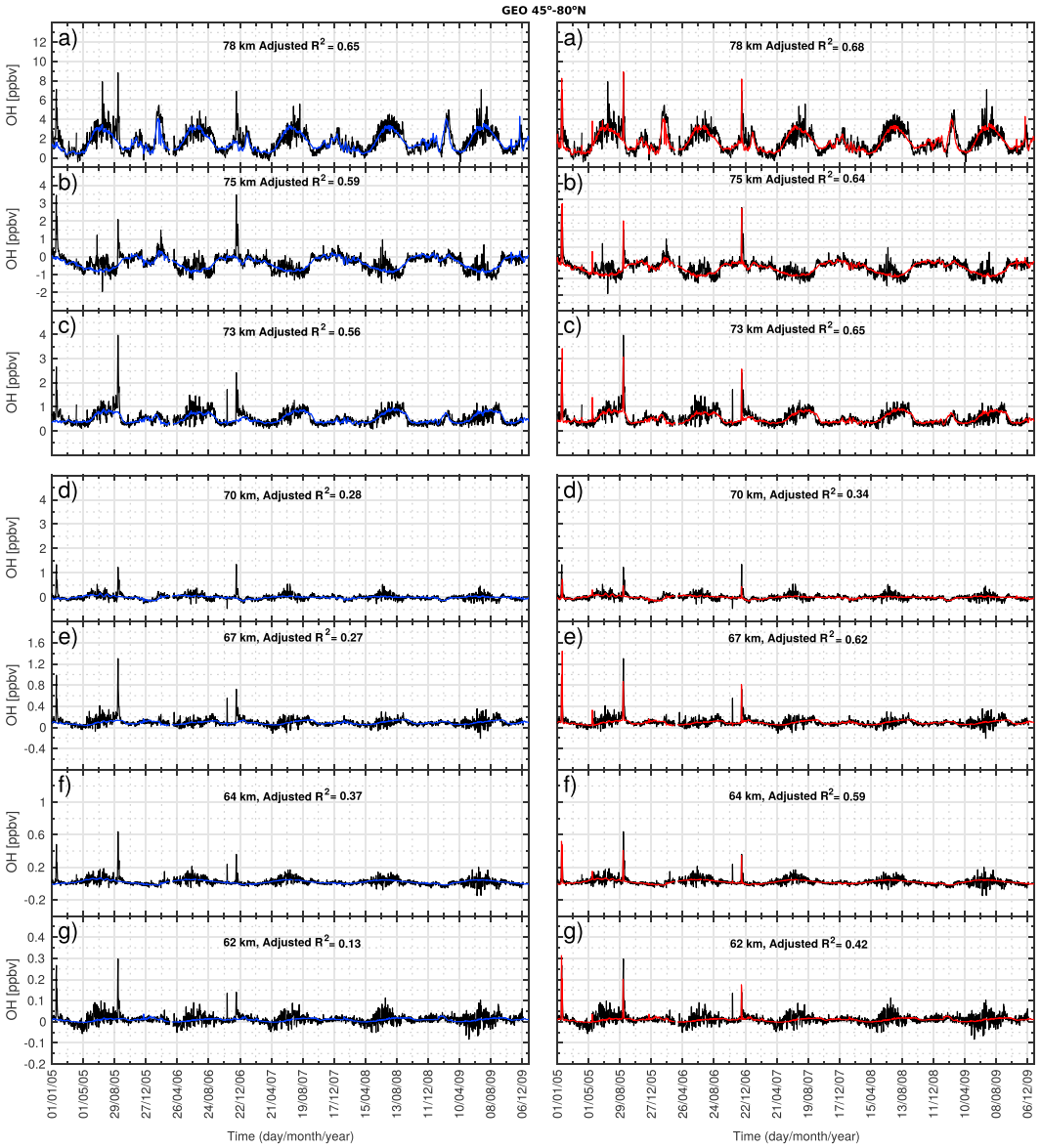

Figure 6. Multiple Linear Regression: Time plots showing observed hydroxyl (OH) (black line) against modeled OH for altitudes 62 to 78 km. The blue lines represent modeled background OH variability. The red lines represent modeled background OH including the contribution of energetic particles (electrons and protons). The data are averaged within the geographical (GEO) latitude range of 45–80°N.

In a CGM latitude setting, however, the contribution of electron energy deposition (blue) above 70-km altitude is comparable to that of protons. While the contribution of protons (green) increases with decreasing altitude and maximizes at 67 km. A summary of the regression workflow for obtaining the relative importance of the proposed predictors to the OH variability is shown in Figure 2 by the orange arrows.

3.2.3. Relative Importance

In Figure 4b we can only approximately deduce the contribution of the particle forcing to the variability in OH. In order to investigate the relative contribution of each of the predictors in the regression models, we *predict* OH using the terms for each predictor in the regression model. Then calculate the correlation coefficient, r_i between the observed and model OH, then calculate r_i^2 by squaring r_i. The total r^2_{total} is the sum of the individual r_i^2. Therefore, the contribution of each predictor to the adjusted R^2 is obtained by

$$R_i^2 = \left(r_i^2 / r^2_{\text{total}}\right) * R^2 \tag{6}$$

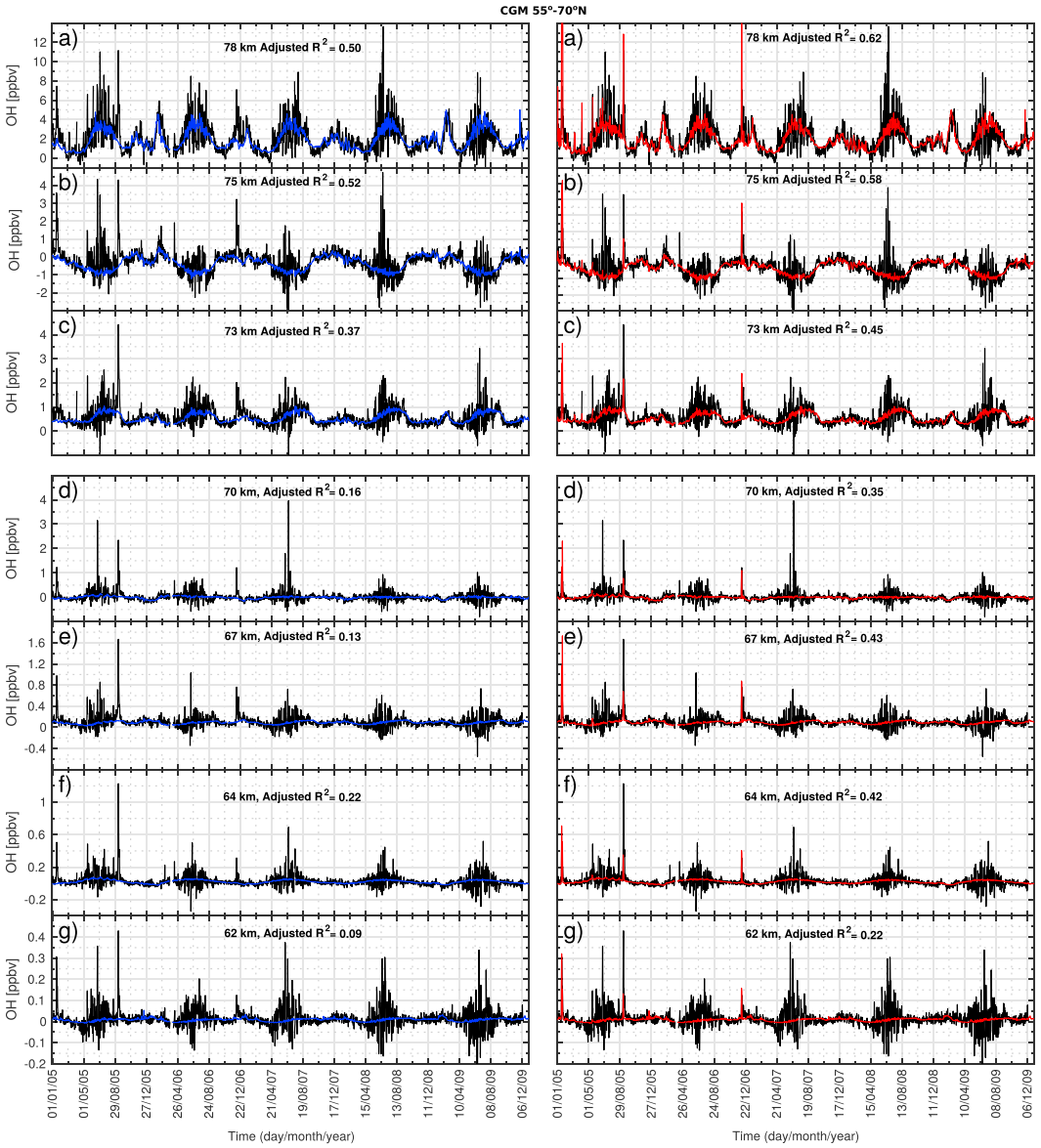

Figure 7. Multiple Linear Regression: Time plots showing observed hydroxyl (OH) (black line) against modeled OH for altitudes 62 to 78 km. The blue lines represent modeled background OH variability. The red lines represent modeled background OH including the contribution of energetic particles (electrons and protons). The data are averaged within a corrected geomagnetic (CGM) latitude range of 55–70°N.

where *i* represents each predictor variable including its higher-order terms if any. Figure 8 shows time plots of the contribution of each predictor variable to the adjusted R^2 for altitude 78 km in a model to which EPP is added. The figure shows the observed OH in black, modeled OH in red (part a), and the contribution of each predictor variable in blue (b–e). H_2O seems to play a dominant role in the background model, with a contribution of about 33% in the geographical setting. Whereas in a CGM setting, temperature seems to dominate with a contribution of 33% at this altitude. SSWs are well approximated by the temperature variability. The particle contribution at this altitide is about 9% and 5% in the geographic and CGM coordinate settings, respectively. This type of breakdown of the contribution of each predictor is done for electrons (EEP), protons (SPEs), and EPP for all altitudes, and the results thereof are shown in Table 5.

The breakdown of the relative importance of the background predictors in an atmosphere that is responding to the total energy deposition (EPP) is shown in Figure 4c and in Table 5. It is evident that temperature and H_2O consistently contribute to OH variability at all altitudes. The I_α^{SZA} and GPH, however, only sporadically

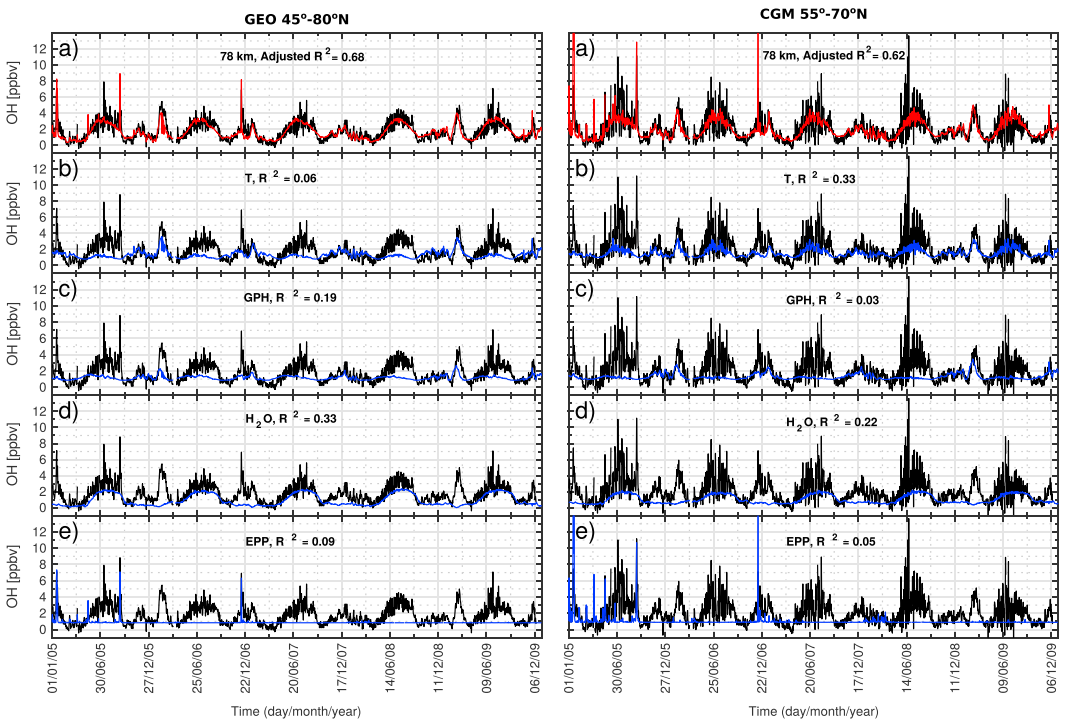

Figure 8. Multiple Linear Regression: Time plots showing observed hydroxyl (OH) (black line) against modeled OH contribution from each of the predictors in the regression model at 78 km. The blue lines represent modeled background OH variability due to at most one predictor in the regression model. The red lines represent modeled OH which includes the background and the contribution of energetic particles (electrons and protons). The data are averaged within the geographical (GEO) latitude range of 45–80°N (left) and within a corrected geomagnetic (CGM) latitude range of 55–70°N (right).

contribute to OH variability at altitudes 64–70 km and 73–78 km, respectively. Therefore, by considering temperature and H_2O only, H_2O dominates over temperature at altitudes 64–73 and 78 km in a geographic setting with a contribution of up to 33%. Also, H_2O dominates over temperature at 64–73 km in a CGM setting with a contribution of up to 22%. At 78-km altitude in a CGM setting, temperature dominates over H_2O with a contribution of 33%. The temperature gives the highest contribution with up to 36% and 34% at 75-km altitude in the geographic and CGM coordinate settings, respectively.

Furthermore, to assess the relative importance of EEP, SPEs, and EPP, a line plot of the contribution of each forcing is shown in Figure 4d. For a geographic setting, electrons contribute up to 15% at 67-km altitude. The contribution of protons increases with decreasing altitude with maximum contribution of about 43% at 67-km altitude. The trend of EPP is the same as that due to SPEs with little difference in values. In a CGM setting, the electron contribution maximizes at 67 and 75 km with a contribution of about 11%. Protons contribute up to 32% at 67 km. The trend of EPP generally follows that of SPEs at all altitudes with maximum contribution of about 34% at 67 km.

Note that there may be a discrepancy of up to ±2% between the total contribution from the predictors and the adjusted R^2. This is probably due to rounding off errors.

4. Discussion

4.1. Mechanisms Directly Driving OH Background Production

Nighttime mesospheric background OH has two main sources: remnants of the daytime production and the reaction of O_3 with atomic hydrogen (H). During normal, unperturbed conditions in the mesosphere, OH is mainly produced through photodissociation of H_2O by the reaction given by equation 1. The chemical lifetime of HO_X is of the order of 0.1 to 1 day in the mesosphere, allowing for the existence of the remnant of daytime OH production after sunset (see Pickett et al., 2006).

Table 5
Multiple Linear Regression: The Contribution of the Various Predictor to the Amount of Variation in OH Explained by the Regression Models for Altitudes 62 to 78 km in the Northern Hemisphere

	Alt	GEO						CGM					
	(km)	*T*	*G*	*H*	*I*	*E*	R^2	*T*	*G*	*H*	*I*	*E*	R^2
	78	0.06	0.21	0.38		0.04	0.69	0.31	0.03	0.21		0.03	0.58
	75	0.38		0.15		0.08	0.61	0.35		0.10		0.11	0.56
	73	0.17	0.04	0.29		0.10	0.60	0.13	0.03	0.20		0.07	0.43
EEP	70	0.03		0.06	0.10	0.10	0.28	0.02		0.03	0.07	0.06	0.18
	67	0.05		0.11	0.00	0.15	0.31	0.02		0.04	0.00	0.11	0.18
	64	0.02		0.10	0.17	0.08	0.37	0.02		0.06	0.09	0.07	0.24
	62	0.06		0.04	0.00	0.05	0.15	0.05		0.02	0.00	0.03	0.11
	78	0.07	0.19	0.32		0.08	0.67	0.28	0.02	0.18		0.04	0.53
	75	0.36		0.13		0.13	0.63	0.35		0.09		0.13	0.56
	73	0.16	0.04	0.28		0.15	0.64	0.13	0.03	0.19		0.08	0.43
SPE	70	0.03		0.05	0.08	0.19	0.34	0.03		0.05	0.10	0.16	0.35
	67	0.05		0.12	0.00	0.43	0.61	0.03		0.06	0.00	0.32	0.41
	64	0.02		0.11	0.19	0.26	0.59	0.02		0.08	0.13	0.18	0.40
	62	0.07		0.05	0.00	0.30	0.41	0.05		0.02	0.00	0.15	0.22
	78	0.06	0.19	0.33		0.09	0.68	0.33	0.03	0.22		0.05	0.62
	75	0.36		0.14		0.14	0.64	0.34		0.09		0.16	0.58
	73	0.16	0.04	0.28		0.16	0.65	0.13	0.03	0.19		0.10	0.45
EPP	70	0.03		0.05	0.08	0.19	0.34	0.03		0.05	0.10	0.17	0.35
	67	0.05		0.12	0.00	0.44	0.62	0.03		0.06	0.00	0.34	0.43
	64	0.02		0.11	0.19	0.27	0.59	0.02		0.08	0.13	0.19	0.42
	62	0.07		0.05	0.00	0.30	0.42	0.05		0.02	0.00	0.15	0.22

Note. Also shown is the adjusted R^2 for regression models for each altitude. The acronyms EEP, SPE, and EPP stand for the electron, protons, and total (electrons plus protons) energy deposition. The letters *T*, *G*, *H*, *I*, and *E* represent the contribution due to the predictors temperature, GPH, H_2O, I_α^{SZA}, and energy deposition, respectively. The variables GPH, H_2O and I_α^{SZA} are: geopotential height, water vapor and solar Lyman alpha radiation as a function of the solar zenith angle, respectively. The acronyms GEO and CGM represent: geographic and corrected geomagnetic, respectively.

The nighttime temperature, GPH, H_2O, and I_α^{SZA} shown in Figure 1 depict clear seasonal variations which are also reflected in the OH VMR, although not so distinctly. The seasonal cycle in the mesospheric temperature, GPH, and H_2O is related to the meridional circulation pattern which is characterized by upwelling at the summer pole, transport of air from the summer pole to the winter pole, causing piling of mass and descent at the winter pole. Adiabatic upward motion of air causes expansion and cooling and also brings up air rich in H_2O from lower altitudes. Adiabatic downward displacement causes compression and warming, and also the descent of dry air from thermospheric altitudes. The descent and ascent of pressure surfaces during winter and summer respectively is seen in Figure 1 in the second panels from top (i.e., GPH). Hence, during summer the mesospheric temperatures are low but the air is rich in H_2O implying more production of OH through photodissociation of H_2O by solar Ly-α radiation which is also high during summer at upper mesospheric altitudes (above 70 km). During winter, the temperatures are high but the H_2O is low, hence low background production of OH. However, the NH high-latitude winter is associated with dynamical processes involving even higher than normal winter time temperatures (>220 K) and increases in the background OH production for example during January 2006, 2007, and 2009 in Figure 1.

The temperature is dynamically connected to GPH and H_2O, and they are anticorrelated as evident in Figure 1 (top 2 panels). Temperature is also anticorrelated with I_α^{SZA}. Figure 3 (top panels) shows that generally temperature is negatively correlated with OH in the mesosphere, except at 75-km altitude. There are, however, periods in winter during which temperature shows a positive correlation with OH. One such example is January to middle March 2009 in the NH corresponding to the 2009 record breaking Arctic SSW during which the polar vortex split, resulting in a greater impact on the lower stratosphere than any other previously observed SSW

with no siginificant recovery of the vortex in that region (Manney et al., 2009). From Figure 1, the high temperatures also correspond to low GPH and low H_2O VMR at the same altitude. This event is preceded by a period during which the OH abundances are low, corresponding to low temperatures, high GPH, and inappreciable change in H_2O VMR.

Planetary wave activity at high latitudes during winter is associated with these temperature enhancements and are known to cause descent of thermospheric dry air, as well as atomic oxygen (O) and H to mesospheric altitudes (see, e.g., Damiani et al., 2010; Zawedde et al., 2016). The O will participate in a three body reaction with O_2, creating O_3 which reacts with H to form vibrationally excited OH (OH^*) by the reaction (Winick et al., 2009):

$$H + O_3 \rightarrow OH^* + O_2 \tag{7}$$

The OH^* is deactivated either by photon emissions in the Meinel band or by collisional quenching (Brasseur & Solomon, 2005). Therefore, in addition to photolysis of H_2O by solar radiation, SSWs and the related planetary wave activity drive mechanisms that enhance OH.

Models with only linear terms failed to capture the variability in OH due to SSWs. The linear terms in the models estimate well the OH background seasonal variability, whereas the quadratic terms estimate well the OH variability due to SSWs. Models with quadratic terms, therefore, successfully accounted for both long- and short-term variations of the background enabling the assessment of the importance of EPP-driven OH production.

4.2. EPP-Driven OH Production

Figure 1, third panels, shows the energy deposition for data averaged over a geographic latitude band of 45–80°N and a CGM latitude band of 55–70°N. The solar energetic protons would precipitate over the entire polar cap. Hence, the impact region would cover a large part of the geographical latitude band of 45–80°. Whereas the latitude range of Earth's radiation belts related to energetic electrons is well approximated by the CGM latitude band of 55–70° . Compared to the entire polar cap, the latitude range of the radiation belts is a small band within the NH. As such, the results would be biased by the dominant type of particle forcing if only one of the latitude bands is considered. Generally for modeling the background OH variability, *geographic* models seem to explain a lot more variability in OH than their *CGM* counterparts, the improvement ranging from 4% to 19% within the mesosphere by comparing Figures 6 and 7 (blue plots). This may be because the parameters responsible for OH background production are oriented in a geographic coordinate system rather than a magnetic coordinate system.

It is well known that EPP leads to production of odd hydrogen of which OH is part. With the availability of OH data from the Aura satellite, the effects of the strong infrequent SPEs have been extensively studied even over the years in question (see, e.g., Damiani et al., 2008; Verronen et al., 2006, 2007). There has also been several more recent studies on the direct EEP impact on OH (see, e.g., Andersson et al., 2012; Andersson, Verronen, Rodger, Clilverd, & Wang 2014; Verronen et al., 2011; Zawedde et al., 2016). It is, however, difficult to find convincing observational evidence of OH increases associated with precipitating electrons at altitudes below 70 km especially during solar minimum years (see, e.g., Verronen et al., 2011, 2013). With multiple linear regression, we show that there is significant and quantifiable OH changes due to EEP even below 70 km associated with relativistic electrons, which is separable from the background production. We find that in a CGM coordinate setting, for example, EEP contributes up to 11% to the OH variability at 67 km. This estimate is 0.92 times the correlation of $r \geq 0.35$ ($r^2 \geq 0.12$ or 12%) between OH mixing ratios and precipitating electrons reported by Andersson et al. (2012) for the altitude 52–70 km, that is, at altitudes affected by 100 keV–3 MeV electrons. Correlation between a single predictor and OH may, however, not necessarily imply causality and correlation analysis does not account for other sources of OH variability.

A number of publications have discussed whether precipitation of electrons from the radiation belt can have a large impact on the composition of the mesosphere comparable to SPEs (see, e.g., Andersson, Verronen, Rodger, Clilverd, & Seppälä 2014). EEP events are weaker, and their chemical response is hard to detect but occurs much more frequently than the strong sporadic SPEs. Nevertheless, the weak geomagnetic storms associated with EEP during solar minimum produce local OH enhancements that are comparable to the OH enhancements due to background atmospheric dynamics (see, e.g., Zawedde et al., 2016). In order to understand and quantify the effect of EEP on mesospheric OH, we model the background OH variability, taking into account all the possible sources of OH variability as given in Table 3. Furthermore, the contribution of each

predictor variable to the adjusted R^2 is estimated by equation (6) as described in subsection 3.2.3 and listed in Table 5. At 78 km for example, temperature, GPH, H_2O, I_α^{SZA}, and EPP contribute 6%, 19%, 33%, 0%, and 9% respectively for a geographic setting, with an adjusted R^2 of 68%. These numbers will slightly vary depending on the kind of particle forcing included in the regression model. It is clear that H_2O dominates the background OH production at this altitude. For a CGM setting at 78 km, temperature, GPH, H_2O, I_α^{SZA}, and EPP contribute 33%, 3%, 22%, 0%, and 5% respectively (see Figure 8).

Considering all altitudes, GPH exhibits a sporadic contribution at 73- to 78-km altitude, which weakens in a CGM setting. The I_α^{SZA} contribution though sporadic, dominates at 64- to 70-km altitude (see Figure 4c). While temperature and H_2O show consistent contribution to OH variability at all altitudes and hence are the dominant contributors. Temperature plays a dominant role at 75 km where it exhibits maximum contribution to OH variability. As mentioned earlier this altitude has a reverse seasonal behavior to that exhibited by other mesospheric altitudes. H_2O seemed to be the main contributor to OH variability at altitudes 64–73 km. Generally, temperature dominates OH variability in the upper mesosphere while in the lower mesosphere, H_2O dominates over temperature. The dominance of temperature over H_2O in the upper mesosphere (75–78) for the *CGM* models (Figure 4c, red line) is consistent with the Sodankylä Ion and Neutral Chemistry (SIC) model runs for March 2008 for altitudes 65–75 km at 60°N/S by Andersson et al. (2012) performed to verify the sensitivity of OH to H_2O and temperature. These model runs, however, do not include particle precipitation.

H_2O is important for the background OH production through photolysis, it may also be important for the dynamical OH production since it is dynamically connected to temperature. Further, H_2O is important for the EPP-OH production because it is an important constituent for formation of water cluster ions. Mesospheric HO_X, regardless of its source, can be converted to molecular hydrogen (H_2) by the reaction (Crutzen & Solomon, 1980):

$$H + HO_2 \rightarrow H_2 + O_2 \tag{8}$$

For EPP, this effect is most pronounced in the altitude range 70–85 km, thus temporarily resulting in enhanced conversion of H_2O to H_2 after an event. This results in a nonlinear relationship between OH and EPP. Therefore, with simple linear regression alone, it is not possible to clearly distinguish between the different pathways H_2O can affect the OH production.

In case of strong precipitation events, the H_2O cluster reactions which occur during EPP-HO_X production may be obstructed by dissociative recombination of the intermediate positive ions with electrons, resulting in lower HO_X production rate (<2 radicals) during periods of elevated electron concentrations (Solomon et al., 1981). This process may be expedited if the H_2O mixing ratios become less than a few parts per billion (ppb). In that case, even the natural electron concentration may considerably reduce the efficiency of HO_X production through water cluster reactions. The Solomon et al. (1981) Figure 2 shows that HO_X production rate decreases with increasing ionization rate and also decreases with increasing altitude (see also Sinnhuber et al., 2012). The decrease of EPP-HO_X production rate is hence strongly dependent on H_2O which in turn is modulated by season, latitude, and the rate of vertical transport. Therefore, it is reasonable to assume that in our regression analysis the overestimation of OH production during periods of intense precipitation events is due to this nonlinear relationship between the ionization rate and the HO_X production rate. This effect is seen in Figures 6 and 7 for the red plots especially for altitudes 75 and 78 km. At 75 km, for example, considering the January 2005 SPE, the models shown in Figures 6 and 7 overestimate the OH VMR by ~6% and ~40% for the geographic and CGM latitude bands, respectively. The peak ionization rates of 734 $cm^{-3}s^{-1}$ and 730 $cm^{-3}s^{-1}$ (not shown) associated with this event in the geographic and CGM coordinate settings are consistent with a HO_X production per ionization of ~1.7–1.8 at 75 km (see Solomon et a., 1981). These production rates are 10–15% lower than the assumed $2HO_X$ per ionization.

Andersson, Verronen, Rodger, Clilverd, and Seppälä (2014) argue that although the duration of the forcing for individual EEP events is only a few days, the high frequency of occurrence of EEP events is enough to cause variability in mesospheric O_3 on solar cycle time scales. For years 2005 to 2009, our results show that in the mesosphere, electrons contribute up to 11% variability in OH in a CGM coordinate setting (Figure 4d, blue), which is not directly comparable to the estimate (9%) from Andersson, Verronen, Rodger, Clilverd, and Seppälä (2014) for O_3 depletion since OH cataltytically deplets O_3. The difference might also be due the fact that we are considering a wider latitude band (55–70°) than that (55–65°) by Andersson, Verronen, Rodger, Clilverd, and Seppälä (2014). Further, Figure 4c is for the NH, while the Andersson, Verronen, Rodger, Clilverd, and Seppälä (2014) Figure 3c shows the Southern Hemisphere. They looked at the EEP impact by contrasting

periods of maximum and minimum EEP activity, which they considered as an indication of the maximum variability during the solar cycle, while we use multiple linear regression to investigate the contribution from a predictor variable when other variables are held constant.

The relative contribution of EEP, SPEs, and EPP is shown in Figure 4d. For the geographic setting, the relative contribution from electrons maximizes at 67-km altitude with a contribution of 15%. But still this is much lower than the maximum contribution of protons which is up to ~43% at 67 km. Protons dominate over electrons in the contribution to OH production in a geographic coordinate system setting as protons precipitate over the entire geographic band in question, whereas electrons precipitate within a limited region connected to the Earth's radiation belts (see, e.g., Andersson, Verronen, Rodger, Clilverd, & Wang 2014). In a CGM coordinate system, which follows the latitude range of Earth's radiation belts, EEP contribution to the OH variability is comparable to that of SPEs for altitudes above 70 km with a contribution of 11% at 75 km. This is consistent with 50- to 200-keV electrons which deposit most of their energy within 70–78 km (see, e.g., Andersson et al., 2012; Turunen et al., 2009). Relativistic electrons (>200 keV) deposit their energy below 70 km where the EEP impact exhibits maximum contribution of up to 11% at 67 km. Protons contribute most below 70 km with maximum contribution of 32% which also occurs at 67 km. The EPP profile generally resembles the proton profile for all altitudes with two distinct maxima at 67 and 75 km. These maxima correspond to contributions of 34% and 16%, respectively.

In general, over the declining and minimum phase of the solar cycle 23, the background parameters are responsible for most of the OH variability in the upper mesosphere above 70 km. For altitudes 62–70 km, however, EPP (and SPEs) seems to contribute more than any of the other predictors in the respective regression models (see Figures 4c and 4d). EEP dominates over the background at 67 km in both the geographic and CGM coordinate setting, respectively. Therefore, the derived effectiveness of a particle source in contributing to variability of OH depends on the type of coordinate system one is working in, as well as the energy of the incident particles which will ultimately determine the altitude at which the energy will be deposited.

4.3. On Shorter Time Scales

A long time series, including different phases of the solar cycle, is required when assessing the relative importance of EEP and SPEs upon OH in general. The lack of SPEs and the lower intensity of the EEP during solar minimum implies, however, that the role of EPP with respect to the background variability will be damped as the background variability is much less affected by the solar cycle phases. For completeness, we wish therefore to demonstrate how the methodology works on shorter time scales.

We apply the methodology in subsections 3.2.2 and 3.2.3 focusing solely on the more active years 2005–2006, where we find most of the EPP activity both in regard to SPEs and EEP. Figure 9 shows the relative contribution of EEP, SPEs, and EPP to the observed OH variability. In this case, the role of EEP in the geographic and geomagnetic latitude bands is up to ~22% and ~20%, respectively. Averaging the OH data over the CGM latitude band introduces short-term variations, most pronounced during summer, with features that are neither captured by the background variability nor by EEP. There is, nevertheless, an improvement of up to 7% in the EEP contribution at 75-km altitude due to changing to the CGM setting. It is also evident that EPP in general now is responsible for 14–60% of the OH variability between 62- and 78-km altitude.

Further, the methodology can also be used to target the relative importance of the different parameters on for example seasonal time scales. In particular, EPP-induced ozone loss during late winter and early spring has been considered as a candidate for influencing the meridional temperature change and subsequently the upward wave propagation. This could potentially impact the atmospheric dynamics from the lower mesosphere, stratosphere, and all the way to the ground (e.g., Seppälä et al., 2009, 2013). Figure 10 shows the breakdown of the contribution of the various predictors to the modeled OH variability at 78 km during February to April 2005 and 2007. The OH background level is impacted by the spring transition at the end of the periods, as well as individual EEP events. For these two case studies, EEP contributes 30–34% to the modeled OH. The contribution from EEP is more than the background contribution at 78 km. At the other altitudes, the background generally contributes more than EEP (not shown), except at 73 km for 2005.

A detailed analysis of the relative importance of EPP and the background analysis at different time scales are, however, out of scope of the current study as the main objective is to shed light on the relative importance of EEP and SPEs which requires a long time series. It demonstrates, however, the potential of a multiple linear regression model to contribute to also other important questions regarding EPP effect on OH.

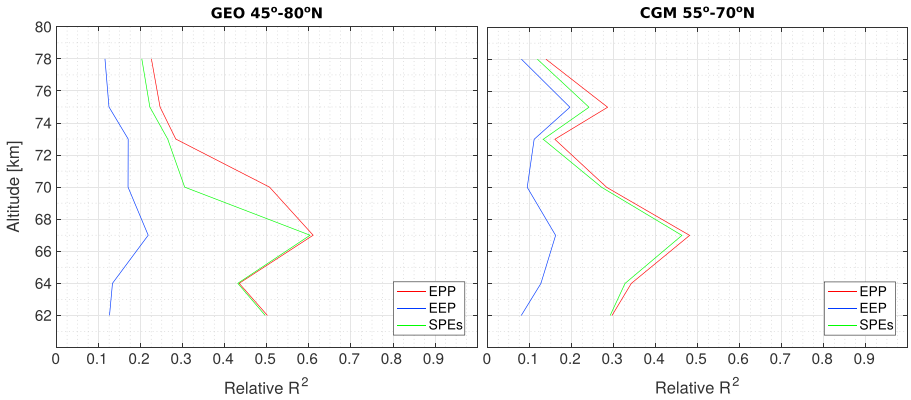

Figure 9. Multiple Linear Regression: Relative contribution of EEP, SPEs and EPP for years 2005-2006 for the geographical latitude band (45° -80° N) and CGM latitude band (55° – 70° N). The red, blue and green lines represent EPP, EEP and SPEs respectively.

4.4. Comparison to Other Studies

In one of the earliest review studies, Thorne (1980) assesses the relative contribution of certain classes of EPP to the chemical composition of the middle atmosphere. He stresses the production of odd nitrogen (NO_X) and HO_X and their subsequent role in catalytic destruction of O_3. Using the August 1972 SPE, Thorne (1980) shows that the effect of this event peaks at ~50 km with up to 50% reduction in O_3. Such depletions of polar O_3 should cause a net reduction in the heating rate of 2.5° K/day at 60 km and 1.3° K/day at 45 km (under sunlit conditions). Thorne (1980) also combines ionization rates during two intense Relativistic Electron Precipitation events with cluster ion chemistry results to obtain profiles for mesospheric HO_X production, which he compares to the two major quiet time sources of HO_X. From that study it is evident that electron precipitation can provide an important contribution over a broad altitude range near 70 km within the mesosphere which behavior is also seen in our analysis in Figure 4d.

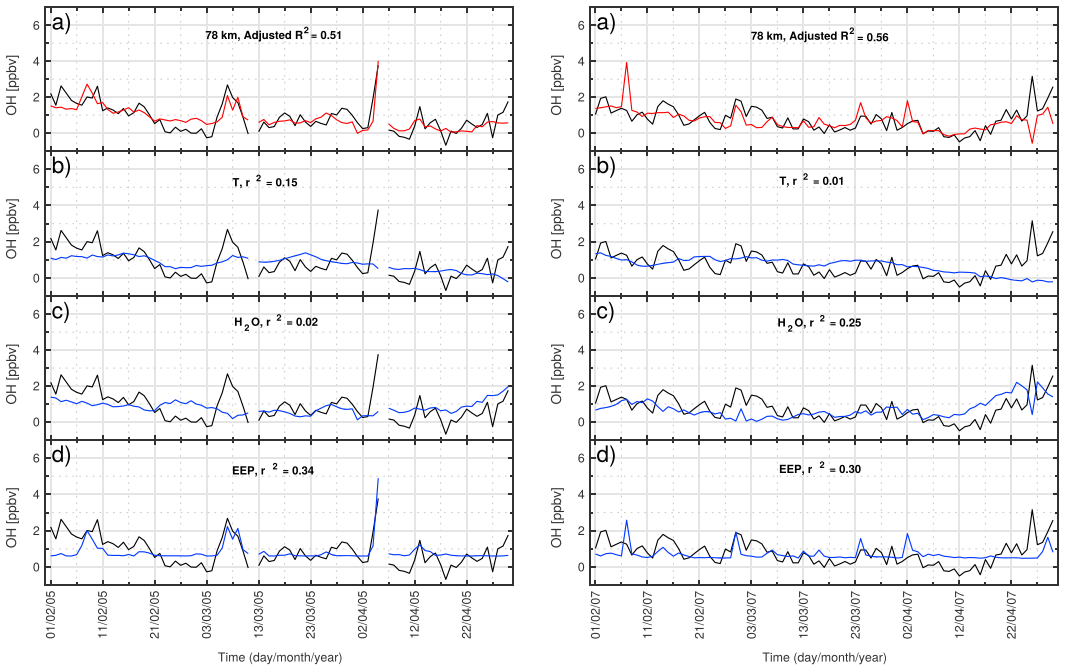

Figure 10. Multiple Linear Regression: Time plots showing observed OH (black line) against modeled OH contribution from each of the predictors in the regression model at 78 km for the spring transitions in 2005 (left) and 2007 (right). The blue lines represent modeled background OH variability due to at most one predictor in the regression model. The red lines represent modeled OH which includes the background and the contribution of energetic electron precipitation. The data are averaged within the CGM latitude range of 55° – 70°N.

On a diurnal scale, Aikin and Smith (1999) model the response of mesospheric constituents to EEP for two precipitation scenarios for altitudes 65, 70, and 75 km. They report that at high latitudes OH and HO_2 concentrations are enhanced by electron energy deposition with the largest difference between the background and EEP-induced OH and HO_2 occurring in the early morning hours. They stress that during the day, the extent of enhancement depends on overcoming the background production which is proportional to the ambient H_2O mixing ratio. For our study, however, we use only nighttime data for all the analysis mainly to ensure a low OH background that will enable easier detection of EEP induced OH.

Verronen et al. (2013) select the four strongest EEP events that occurred during the period 2004 to 2009: January, March; May 2005 and April 2006 and use the SIC model to study the effect of radiation belt electron precipitation on mesospheric OH and O_3 from Aura MLS. They show that the magnitude of EEP-induced OH increase depends on the SZA and the level of the background OH production with the largest OH increase seen in the winter pole at around sunrise as also reported by Aikin and Smith (1999). The OH enhancements reported in this study led to several tens of percent depletion to O_3, which was comparable to the effects previously reported in cases of large SPEs. Although the SIC model was able to reproduce the observed daily variability of OH and O_3 at 70- to 80-km altitude, they report significant differences in the absolute OH concentrations in the lower mesosphere. This implied that some correction might be needed for energies >300 keV in order to make confident conclusions at lower altitudes. With our current study, however, we have incorporated the necessary corrections for proton contamination of the electron channels and also accounted for relativistic electrons (>757 keV) which deposit their energy in the lower mesosphere as described in Nesse Tyssøy et al. (2016).

Verronen et al. (2015) use the electron concentration observations of the European Incoherent Scatter scientific Association incoherent scatter radars located in Tromsø to investigate the contribution of proton and electron precipitation to the observed electron density in the mesosphere-lower thermosphere during the October–November 2003 and September 2005 SPEs. They compare European Incoherent Scatter scientific Association measurements to the results from the SIC model, designed to separate the effects of protons and electrons. Using proton and electron ionization rates calculated from the Atmospheric Ionization Model Osnabrück v1.2, Figure 1 in Verronen et al. (2015) generally shows that protons dominate over electrons at lower altitudes (below ~72 km for September 2005 SPE) and electrons dominate at higher altitudes. This trend is also exhibited by our results in Figure 4b. Although there are similar trends for the electron and proton contribution, this differs from our study in the following ways: First as already mentioned, the source of the particle forcing differs in that we use both SPEs and EEP events for the period 2005 to 2009 in our analysis whereas Verronen et al. (2015) use two SPEs as the source of proton and electron precipitation. Then the ultimate effect and altitude of the particle precipitation is different for both studies, we are interested in effects on mesospheric chemistry, while they are interested in ionospheric effects. Furthermore, due to proton contamination of the POES MEPED electron detectors, the Atmospheric Ionization Model Osnabrück v1.2 electron ionization seems to be overestimated during SPEs forcing below 90 km where our region of interest in located. As already stated, NOAA POES data challenges are catered for as described in Nesse Tyssøy et al. (2016) for this study.

Overall, we find that in both geographic and CGM coordinate settings, the SPEs contribution to the OH variability dominates over that due to electrons for all altitudes. We find that the magnitude of the electron contribution from this study is less than that from other studies, for example, by Verronen et al. (2011) and Andersson et al. (2012) possibly due to the fact that those studies use correlation analysis without accounting for the presence of other sources of OH variability. Furthermore, some of these studies investigate case studies of very active periods which provide the short-term EEP effects on mesospheric OH and consequently on O_3. With this multiple linear regression, we investigate the relative contribution from the different available sources (or parameters) to the observed nighttime OH variability during 2005 to 2009, covering the declining and minimum phase of the solar cycle 23.

5. Summary and Conclusions

We model the natural background variability in nighttime OH using multiple linear regression, taking into account the temperature, GPH, H_2O, and I_{α}^{SZA}. Using the new MEPED analysis toolkit, we estimate the particle energy deposition in the mesosphere. We then add the different kinds of particle energy deposition (i.e., EEP, SPEs, and EPP) separately to the background regression model resulting in three types of models.

Our results show the breakdown of the contribution from the various sources to OH variability, giving the relative importance of these sources in the mesosphere.

Our models are able to capture both seasonal variations as well as short-term variability such as SSWs. Generally, temperature and H_2O seem to consistently contribute to OH variability and hence are considered the most important contributors to mesospheric background OH variability. By comparing temperature and H_2O profiles, H_2O seems to be a dominant contributor to the background OH production at altitudes 64–73 km in both coordinate settings. Temperature dominates at 75-km altitude with maximum contribution of 38% and 35% in the geographic and CGM settings, respectively.

Further, we have evaluated the role of EPP and the relative importance of EEP and SPEs over the declining and minimum phase of the solar cycle 23. However, the derived effect of energetic particles on OH depends on the applied coordinate system as well as the altitude range in consideration. In a geographic coordinate setting, protons dominate over electrons at all altitudes with a maximum contribution to OH variability of ∼43% at 67 km. In a CGM coordinate setting, protons dominate over electrons only below 70 km with a maximum contribution to OH variability of ∼32%. Above 70 km, the electrons contribution is comparable to the protons contribution to OH variability, with maximum contribution of ∼11% at 75 km. Note that the numbers given refers to the NH. Applying the methodology in the Southern Hemisphere should, however, not impact the conclusion regarding the relative importance of SPEs and EEP. It might, on the other hand, affect relative importance of the background parameters and EPP due to a larger offset between the geographic and geomagnetic coordinate system. This should be explored in a future study.

Generally, the background dominates over the particles above 70-km altitude over the period considered. However, for altitudes below 70 km, the relative contribution from EPP is more than the relative contribution from any of the background predictors. The relative contribution of EEP and SPEs depends on the coordinate system of interest and also the energy of the incident particles which determines the altitude of the energy deposition.

The period 2005 to 2009 considered in this study coincided with the latter less active part of the declining phase of solar cycle 23. The years 2008–2009 were exceptionally quiet in regard to EPP in general. Therefore, the results from this study give a lower estimate of the relative contribution of EEP and SPEs to OH variability over the declining phase of solar cycle 23. To get a more general picture, longer time series encompassing the entire declining phase or even larger periods should be considered.

Acknowledgments
This study was supported by the Research Council of Norway under contract 223252/F50. The authors thank the NOAA's National Geophysical Data Center (NGDS) for providing NOAA POES data (https://satdat.ngdc.noaa.gov/), the LASP Interactive Solar IRradiation Datacenter (LISIRD) for providing composite solar Lyman alpha data (http://lasp.colorado.edu/lisird/lya/), and NASA Goddard Earth Science Data and Information Services Center (GES DISC) for providing Aura/MLS data (https://mls.jpl.nasa.gov/).

References

Aikin, A. C., & Smith, H. J. P. (1999). Mesospheric constituent variations during electron precipitation events. *Journal of Geophysical Research: Atmospheres*, *104*(D21), 26,457–26,471. https://doi.org/10.1029/1999JD900752

Andersson, M. E., Verronen, P. T., Rodger, C. J., Clilverd, M. A., & Seppälä, A. (2014). Missing driver in the Sun-Earth connection from energetic electron precipitation impacts mesospheric ozone. *Nature Communications*, *5*(5197). https://doi.org/10.1038/ncomms6197

Andersson, M. E., Verronen, P. T., Rodger, C. J., Clilverd, M. A., & Wang, S. (2014). Longitudinal hotspots in the mesospheric OH variations due to energetic electron precipitation. *Atmospheric Chemistry and Physics*, *14*(2), 1095–1105. https://doi.org/10.5194/acp-14-1095-2014

Andersson, M. E., Verronen, P. T., Wang, S., Rodger, C. J., Clilverd, M. A., & Carson, B. R. (2012). Precipitating radiation belt electrons and enhancements of mesospheric hydroxyl during 2004–2009. *Journal of Geophysical Research: Atmospheres*, *117*, D09304. https://doi.org/10.1029/2011JD017246

Belsley, D. A., Kuh, E., & Welsch, R. E. (2005). *Detecting and assessing collinearity* (pp. 85–191). John Wiley & Sons, Inc. https://10.1002/0471725153.ch3

Bethe, H. A., & Ashkin, J. (1953). *Part II of experimental nuclear physics, Passage of radiations through matter* (Vol. 1). New York: John Wiley & Sons.

Brasseur, G. P., & Solomon, S. (2005). *Aeronomy of the middle atmosphere: Chemistry and physics of the stratosphere and mesosphere.* Netherlands: Springer.

Canty, T., & Minschwaner, K. (2002). Seasonal and solar cycle variability of OH in the middle atmosphere. *Journal of Geophysical Research: Atmospheres*, *107*(D24), 4737. https://doi.org/10.1029/2002JD002278

Crutzen, P. J., & Solomon, S. (1980). Response of mesopheric ozone to particle precipitation. *Planetary and Space Science*, *28*(12), 1147–1153. https://doi.org/10.1016/0032-0633(80)90073-2

Daae, M., Espy, P., Nesse Tyssøy, H., Newnham, D., Stadsnes, J., & Søraas, F. (2012). The effect of energetic electron precipitation on middle mesospheric night-time ozone during and after a moderate geomagnetic storm. *Geophysical Research Letters*, *39*, L21811. https://doi.org/10.1029/2012GL053787

Damiani, A., Storini, M., Laurenza, M., & Rafanelli, C. (2008). Solar particle effects on minor components of the polar atmosphere. *Annales Geophysicae*, *26*(2), 361–370.

Damiani, A., Storini, M., Santee, M. L., & Wang, S. (2010). Variability of the nighttime OH layer and mesospheric ozone at high latitudes during northern winter: Influence of meteorology. *Atmospheric Chemistry and Physics*, *10*(21), 10,291–10,303. https://doi.org/10.5194/acp-10-10291-2010

Evans, D., & Greer, M. (2000). *Polar orbiting environmental satellite space environment monitor—2: Instrument descriptions and archive data documentation* (1.4). Boulder, CO: Space Environment Center.

Frederick, J. E., & Hudson, R. D. (1980). Atmospheric opacity in the Schumann-Runge bands and the aeronomic dissociation of water vapor. *Journal of the Atmospheric Sciences*, *55*, 301–327. https://doi.org/10.1175/1520-0469(1980)037<1088:AOITSR>2.0.CO;2

Fritsch, F. N., & Carlson, R. E. (1980). Monotone piecewise cubic interpolation. *SIAM Journal on Numerical Analysis*, *17*(2), 238–246.

Hedin, A. E. (1991). Extension of the MSIS thermosphere model into the middle and lower atmosphere. *Journal of Geophysical Research*, *96*(A2), 1159–1172. https://doi.org/10.1029/90JA02125

Li, X., & Temerin, M. A. (2001). The electron radiation belt. *Space Science Reviews*, *95*, 569–580.

Livesey, N. J., Read, W. G., Wagner, P. A., Froidevaux, L., Lambert, A., Manney, G. L., et al. (2015). *Earth Observing system(EOS) Aura Microwave Limb Sounder(MLS) Version 4.2x Level 2 data quality and description document* (91109-8099, version 4.2x-1.0). Pasadena, California: Jet Propulsion Laboratory, California Institute of Technology.

Manney, G. L., Schwartz, M. J., Krüger, K., Santee, M. L., Pawson, S., Lee, J. N., et al. (2009). Aura Microwave Limb Sounder observations of dynamics and transport during the record-breaking 2009 arctic stratospheric major warming. *Geophysical Research Letters*, *36*(12), L12815. https://doi.org/10.1029/2009GL038586

Minschwaner, K., Manney, G. L., Wang, S. H., & Harwood, R. S. (2011). Hydroxyl in the stratosphere and mesosphere—Part 1: Diurnal variability. *Atmospheric Chemistry and Physics*, *11*(3), 955–962. https://doi.org/10.5194/acp-11-955-2011

Nesse Tyssøy, H., Sandanger, M. I., Ødegaard, L.-K. G., Stadsnes, J., Aasnes, A., & Zawedde, A. E. (2016). Energetic electron precipitation into the middle atmosphere-constructing the loss cone fluxes from MEPED POES. *Journal of Geophysical Research: Space Physics*, *121*, 5693–5707. https://doi.org/10.1002/2016JA022752

Nesse Tyssøy, H., & Stadsnes, J. (2015). Cutoff latitude variation during solar proton events: Causes and consequences. *Journal of Geophysical Research: Space Physics*, *120*, 553–563. https://doi.org/10.1002/2014JA020508

Nesse Tyssøy, H., Stadsnes, J., Søraas, F., & Sørbø, M. (2013). Variations in cutoff latitude during the January 2012 solar proton event and implication for the distribution of particle energy deposition. *Geophysical Research Letters*, *40*, 4149–4153. https://doi.org/10.1002/grl.50815

Ødegaard, L.-K. G., Tyssøy, H. N., Sandanger, M. I. J., Stadsnes, J., & Søraas, F. (2016). Space weather impact on the degradation of NOAA POES MEPED proton detectors. *Journal of Space Weather and Space Climate*, *6*, A26. https://doi.org/10.1051/swsc/2016020

Ødegaard, L.-K. G., Tyssøy, H. N., Søraas, F., Stadsnes, J., & Sandanger, M. I. (2017). Energetic electron precipitation in weak to moderate corotating interaction region-driven storms. *Journal of Geophysical Research: Space Physics*, *122*, 2900–2921. https://doi.org/10.1002/2016JA023096

Pickett, H. M., Read, W. G., Lee, K. K., & Yung, Y. L. (2006). Observation of night OH in the mesosphere. *Geophysical Research Letters*, *33*, L19808. https://doi.org/10.1029/2006GL026910

Rawlings, J. O., Pantula, S. G., & Dickey, D. A. (1998). *Applied regression analysis: A research tool* (second ed.). New York: Springer.

Rees, M. H. (1989). Physics of the upper atmosphere. *Quarterly Journal of the Royal Meteorological Society*, *117*(498), 433–433.

Reeves, G. D., Spence, H. E., Henderson, M. G., Morley, S. K., Friedel, R. H. W., Funsten, H. O., et al. (2013). Electron acceleration in the heart of the Van Allen Radiation Belts. *Science*, *341*(6149), 991–994. https://doi.org/10.1126/science.1237743

Rodger, C. J., Clilverd, M. A., Green, J. C., & Lam, M. M. (2010). Use of POES SEM-2 observations to examine radiation belt dynamics and energetic electron precipitation into the atmosphere. *Journal of Geophysical Research*, *115*, A04202. https://doi.org/10.1029/2008JA014023

Rodger, C. J., Kavanagh, A. J., Clilverd, M. A., & Marple, S. R. (2013). Comparison between POES energetic electron precipitation observations and riometer absorptions: Implications for determining true precipitation fluxes. *Journal of Geophysical Research: Space Physics*, *118*, 7810–7821. https://doi.org/10.1002/2013JA019439

Sandanger, M. I., Ødegaard, L. K. G., Tyssøy, H. N., Stadsnes, J., Søraas, F., Oksavik, K., et al. (2015). In flight calibration of NOAA POES proton detectors—Derivation of the MEPED correction factors. *Journal of Geophysical Research: Space Physics*, *120*, 9578–9593. https://doi.org/10.1002/2015JA021388

Schoeberl, M., Douglass, A., Hilsenrath, E., Bhartia, P., Beer, R., Waters, J., et al. (2006). Overview of the EOS Aura mission. *Geoscience and Remote Sensing, IEEE Transactions on*, *44*(5), 1066–1074. https://doi.org/10.1109/TGRS.2005.861950

Seppälä, A., Lu, H., Clilverd, M. A., & Rodger, C. J. (2013). Geomagnetic activity signatures in wintertime stratosphere wind, temperature, and wave response. *Journal of Geophysical Research: Atmospheres*, *118*, 2169–2183. https://doi.org/10.1002/jgrd.50236

Seppälä, A., Randall, C. E., Clilverd, M. A., Rozanov, E., & Rodger, C. J. (2009). Geomagnetic activity and polar surface air temperature variability. *Journal of Geophysical Research: Space Physics*, *114*, A10312. https://doi.org/10.1029/2008JA014029

Shapiro, A. V., Rozanov, E., Shapiro, A. I., Wang, S., Egorova, T., Schmutz, W., et al. (2012). Signature of the 27-day solar rotation cycle in mesospheric OH and H_2O observed by the Aura Microwave Limb Sounder. *Atmospheric Chemistry and Physics*, *12*(7), 3181–3188. https://doi.org/10.5194/acp-12-3181-2012

Sinnhuber, M., Nieder, H., & Wieters, N. (2012). Energetic particle precipitation and the chemistry of the mesosphere/lower thermosphere. *Surveys in Geophysics*, *33*, 1281–1334.

Solomon, S., Reid, G. C., Rusch, D. W., & Thomas, R. J. (1983). Mesospheric ozone depletion during the solar proton event of July 13, 1982 Part II. comparison between theory and measurements. *Geophysical Research Letters*, *10*(4), 257–260. https://doi.org/10.1029/GL010i004p00257

Solomon, S., Rusch, D., Gérard, J., Reid, G., & Crutzen, P. (1981). The effect of particle precipitation events on the neutral and ion chemistry of the middle atmosphere: II. Odd hydrogen. *Planetary and Space Science*, *29*(8), 885–893. https://doi.org/10.1016/0032-0633(81)90078-7

Swider, W., & Keneshea, T. (1973). Decrease of ozone and atomic oxygen in the lower mesosphere during a PCA event. *Planetary and Space Science*, *21*(11), 1969–1973. https://doi.org/10.1016/0032-0633(73)90126-8

Thorne, R. (1980). The importance of energetic particle precipitation on the chemical composition of the middle atmosphere. *Pure and applied geophysics*, *118*(1), 128–151. https://doi.org/10.1007/BF01586448

Turner, D. L., Shprits, Y., Hartinger, M., & Angelopoulos, V. (2012). Explaining sudden losses of outer radiation belt electrons during geomagnetic storms. *Nature Publishing Group*, *8*(3), 208–212. https://doi.org/10.1038/nphys2185

Turunen, E., Kero, A., Verronen, P. T., Miyoshi, Y., Oyama, S.-I., & Saito, S. (2016). Mesospheric ozone destruction by high-energy electron precipitation associated with pulsating aurora. *Journal of Geophysical Research: Atmospheres*, *121*, 11,852–11,861. https://doi.org/10.1002/2016JD025015JD025015

Turunen, E., Verronen, P. T., Seppälä, A., Rodger, C. J., Clilverd, M. A., Tamminen, J., et al. (2009). Impact of different energies of precipitating particles on NOx generation in the middle and upper atmosphere during geomagnetic storms. *Journal of Atmospheric and Solar-Terrestrial Physics*, *71*(10-11), 1,176–1,189. https://doi.org/10.1016/j.jastp.2008.07.005

Verronen, P. T., Andersson, M. E., Kero, A., Enell, C.-F., Wissing, J. M., Talaat, E. R., et al. (2015). Contribution of proton and electron precipitation to the observed electron concentration in October-November 2003 and September 2005. *Annales Geophysicae*, *33*(3), 381–394. https://doi.org/10.5194/angeo-33-381-2015

Verronen, P., Andersson, M., Rodger, C., Clilverd, M., Wang, S., & Turunen, E. (2013). Comparison of modeled and observed effects of radiation belt electron precipitation on mesospheric hydroxyl and ozone. *Journal of Geophysical Research: Atmospheres*, *118*, 11,419–11,428. https://doi.org/10.1002/jgrd.50845

Verronen, P. T., Rodger, C. J., Clilverd, M. A., Pickett, H. M., & Turunen, E. (2007). Latitudinal extent of the January 2005 solar proton event in the northern hemisphere from satellite observations of hydroxyl. *Annales Geophysicae*, *25*(10), 2203–2215. https://doi.org/10.5194/angeo-25-2203-2007

Verronen, P. T., Rodger, C. J., Clilverd, M. A., & Wang, S. (2011). First evidence of mesospheric hydroxyl response to electron precipitation from the radiation belts. *Journal of Geophysical Research: Atmospheres*, *116*, D07307. https://doi.org/10.1029/2010JD014965

Verronen, P. T., Seppälä, A., Kyrölä, E., Tamminen, J., Pickett, H. M., & Turunen, E. (2006). Production of odd hydrogen in the mesosphere during the January 2005 solar proton event. *Geophysical Research Letters*, *33*, L24811. https://doi.org/10.1029/2006GL028115

Waters, J. W., Froidevaux, L., Harwood, R. S., Jarnot, R. F., Pickett, H. M., Read, W. G., et al. (2006). The earth observing system microwave limb sounder (EOS MLS) on the Aura satellite. *IEEE Transaction Geoscience and Remote Sensing*, *44*(5), 1075–1092. https://doi.org/10.1109/TGRS.2006.873771

Webb, D. (1995). Solar and geomagnetic disturbances during the declining phase of recent solar cycles. *Advances in Space Research*, *16*(9), 57–69. https://doi.org/10.1016/0273-1177(95)00315-6

Weeks, L. H., Cuikay, R. S., & Corbin, J. R. (1972). Ozone measurements in the mesosphere during the solar proton event of 2 November 1969. *Journal of the Atmospheric Sciences*, *29*(6), 1138–1142.

Winick, J. R., Wintersteiner, P. P., Picard, R. H., Esplin, D., Mlynczak, M. G., Russell, J. M., et al. (2009). OH layer characteristics during unusual boreal winters of 2004 and 2006. *Journal of Geophysical Research: Space Physics*, *114*, A02303. https://doi.org/10.1029/2008JA013688

Yando, K., Millan, R. M., Green, J. C., & Evans, D. S. (2011). A Monte Carlo simulation of the NOAA POES medium energy proton and electron detector instrument. *Journal of Geophysical Research: Space Physics*, *116*, A10231. https://doi.org/10.1029/2011JA016671

Zawedde, A. E., Nesse Tyssøy, H., Hibbins, R., Espy, P. J., Ødegaard, L.-K. G., Sandanger, M. I., et al. (2016). The impact of energetic electron precipitation on mesospheric hydroxyl during a year of solar minimum. *Journal of Geophysical Research: Space Physics*, *121*, 5914–5929. https://doi.org/10.1002/2016JA022371